2005

The VLT-UVES Survey for Molecular Hydrogen in High-Redshift Damped Lyman α Systems: Physical Conditions in the Neutral Gas

Raghunathan Srianand
IUCAA, India

Patrick Petitjean
Institut d'Astrophysique de Paris - CNRS, France

Cédric Ledoux
European Southern Observatory, Chile

Gary J. Ferland
University of Kentucky, gary@uky.edu

Gargi Shaw
University of Kentucky, gargi@pa.uky.edu

Mon. Not. R. Astron. Soc. **362,** 549–568 (2005) doi:10.1111/j.1365-2966.2005.09324.x

The VLT-UVES survey for molecular hydrogen in high-redshift damped Lyman α systems: physical conditions in the neutral gas

Raghunathan Srianand,[1⋆] Patrick Petitjean,[2,3⋆] Cédric Ledoux,[4⋆] Gary Ferland[5⋆] and Gargi Shaw[5⋆]

[1]*IUCAA, Post Bag 4, Ganesh Khind, Pune 411 007, India*
[2]*Institut d'Astrophysique de Paris – CNRS, 98bis Boulevard Arago, F-75014 Paris, France*
[3]*LERMA, Observatoire de Paris, 61 Avenue de l'Observatoire, F-75014 Paris, France*
[4]*European Southern Observatory, Alonso de Córdova 3107, Casilla 19001, Vitacura, Santiago, Chile*
[5]*Department of Physics and Astronomy, University of Kentucky, 177 Chemistry/Physics Building, Lexington, KY 40506, USA*

Accepted 2005 June 17. Received 2005 June 12; in original form 2005 January 28

ABSTRACT

We study the physical conditions in damped Lyman α systems (DLAs), using a sample of 33 systems towards 26 quasi-stellar objects (QSOs) acquired for a recently completed survey of H_2 by Ledoux, Petitjean & Srianand. We use the column densities of H_2 in different rotational levels, together with those of C I, C I*, C I**, C II* and singly ionized atomic species to discuss the kinetic temperature, the density of hydrogen and the electronic density in the gas together with the ambient ultraviolet (UV) radiation field. Detailed comparisons are made between the observed properties in DLAs, the interstellar medium (ISM) of the Galaxy and the Large and Small Magellanic Clouds (LMCs and SMCs).

The mean kinetic temperature of the gas corresponding to DLA subcomponents in which an H_2 absorption line is detected, derived from the ortho-to-para ratio (OPR) (153 ± 78 K), is higher than that measured in the ISM (77 ± 17 K) and in Magellanic Clouds (82 ± 21 K). Typical pressure in these components (corresponding to $T = 100$–300 K and $n_{\rm H} = 10$–$200\,{\rm cm}^{-3}$), measured using C I fine-structure excitation, are higher than what is measured along ISM sightlines. This is consistent with the corresponding higher values for $N(H_2, J=2)/N(H_2, J=0)$ seen in DLAs. From the column densities of the high-J rotational levels, we derive that the typical radiation field in the H_2-bearing components is of the order of or slightly higher than the mean UV field in the Galactic ISM. Determination of electron density in the gas with H_2 and C I shows that the ionization rate is similar to that of a cold neutral medium (CNM) in a moderate radiation field. This, together with the fact that we see H_2 in 13–20 per cent of the DLAs, can be used to conclude that DLAs at $z > 1.9$ could contribute as much as 50 per cent star formation rate (SFR) density seen in Lyman break galaxies (LBGs).

C II* absorption line is detected in all the components where H_2 absorption line is seen. The excitation of C II in these systems is consistent with the physical parameters derived from the excitation of H_2 and C I. We detect C II* in about 50 per cent of the DLAs and, therefore, in a considerable fraction of DLAs that do not show H_2. In part of the later systems, physical conditions could be similar to that in the CNM gas of the Galaxy. However, the absence of C I absorption line and the presence of Al III absorption lines with a profile similar to the profiles of singly ionized species suggest an appreciable contribution from a warm neutral medium (WNM) and/or partially ionized gas. The absence of H_2, for the level of metallicity and dust depletion seen in these systems, is consistent with low densities (i.e. $n_{\rm H} \leqslant 1\,{\rm cm}^{-3}$) for a radiation field similar to the mean Galactic UV field.

Key words: galaxies: haloes – galaxies: ISM – quasars: absorption lines – cosmology: observations.

⋆E-mail: anand@iucaa.ernet.in (RS); petitjean@iap.fr (PP); cledoux@eso.org (CL); gary@pa.uky.edu (GF); gargi@pa.uky.edu (GS)

1 INTRODUCTION

Damped Lyman α systems (DLAs) seen in quasi-stellar object (QSO) spectra are characterized by very large neutral hydrogen column densities: $N(\mathrm{H\,I}) \gtrsim 2 \times 10^{20}$ cm^{-2}. Such an amount of neutral gas is usually measured through local spiral discs. The case for DLAs to arise through proto-galactic discs is further supported by the fact that the cosmological density of the absorbing gas at $z_{\rm abs} \sim 3$ is of the same order of magnitude as the cosmological density of stars at present epochs (Wolfe 1995). Moreover, the presence of heavy elements ($Z \sim 1/10\,\mathrm{Z}_{\odot}$) suggests that DLAs are located in over-dense regions where star formation activity takes place (Pettini et al. 1997) and at low and intermediate redshifts, strong metal line systems and DLAs have been demonstrated to be associated with galaxies (e.g. Bergeron & Boissé 1991; Le Brun et al. 1997). It has also been shown that the profiles of the lines arising in the neutral gas show evidence for rotation (e.g. Prochaska & Wolfe 1997). However, hydrodynamical simulations have shown that the high-redshift progenitors of present-day Galactic discs could look like an aggregate of well-separated dense clumps. In fact, the kinematics seen in the absorption line profiles of DLAs could be explained by relative motions of the clumps with little rotation (Haehnelt, Steinmetz & Rauch 1998; Ledoux et al. 1998).

Studying the star formation activities in DLAs is very important for the understanding of galaxy formation in the Universe. Recently, Wolfe et al. (2003a,b, 2004) have shown that, even if DLAs sustain only a moderate star formation activity, they will contribute appreciably to the global star formation rate (SFR) density at high redshifts. The SFR in DLAs can be estimated either by detecting the galaxies responsible for DLAs or by inferring the intensity of the ultraviolet (UV) field in DLAs using the induced excitation of atomic and molecular species. In the latter case, it is important to have a clear understanding of the physical conditions in the gas to derive an accurate estimate of the SFR. In the case of the Galactic interstellar medium (ISM), rotational excitations of H_2 (see Browning et al. 2003, and references therein) and fine-structure excitations of C I, C II, O I and Si II are used to derive the physical state of the absorbing gas (see e.g. Welty et al. 1999). Detecting and studying these transitions in DLAs is the first step towards understanding the physical conditions and hence the star-formation activity in DLAs.

Molecular hydrogen is ubiquitous in the neutral phase of the ISM of galaxies. The formation of H_2 is expected on the surface of dust grains, if the gas is cool, dense and mostly neutral, and from the formation of H^- ions if the gas is warm and dust-free (see e.g. Jenkins & Peimbert 1997; Cazaux & Tielens 2002). As the former process is most likely dominant in the neutral gas associated with DLAs, it is possible to obtain an indirect indication of the dust content in DLAs without depending on extinction and/or heavy element depletion effects. Moreover, by determining the populations of different H_2 rotational levels, it is possible to constrain kinetic and rotational excitation temperatures and particle densities. Effective photo-dissociation of H_2 takes place in the energy range 11.1–13.6 eV through Lyman- and Werner-band absorption lines, and the intensity of the local UV radiation field can, therefore, be derived from the observed molecular fraction. A direct determination of the local radiation field could have important implications in bridging the link between DLAs and star-formation activity at high redshifts.

We have searched for molecular hydrogen in DLA and sub-DLAs at high redshift ($z_{\rm abs} > 1.8$), using Ultraviolet and Visible Echelle Spectrograph (UVES) at the Very Large Telescope (VLT) down to a detection limit of typically $N(H_2) \sim 2 \times 10^{14}$ cm^{-2} (see Ledoux et al. 2003). Out of the 33 systems in our sample, eight have firm and two have tentative detections of associated H_2 absorption lines. In all of the systems, we measured metallicities relative to solar, $[X/H]$ (with either $X =$ Zn, S or Si), and depletion factors of iron, [X/Fe], supposedly on to dust grains. Although H_2 molecules are detected in systems with depletion factor, [Zn/Fe], as low as 0.3, the systems where H_2 is detected are usually amongst those with the highest metallicities and depletion factors. In particular, H_2 is detected in the three systems with the largest depletion factors. Moreover, in two different systems, one of the H_2-detected components has [Zn/Fe] >1.5. This directly demonstrates that a large amount of dust is present in the components where H_2 is detected. The mean H_2 molecular fraction, $f = 2N(H_2)/[2N(H_2) + N(\mathrm{H\,I})]$, in DLAs is generally small (typically $\log f < -1$) and similar to what is observed in the Magellanic clouds. There is no correlation between the amount of molecules and the neutral hydrogen column density; in particular, two systems where H_2 is detected have $\log N(\mathrm{H\,I}) < 20.3$. Approximately, 50 per cent of the systems have $\log f < -6$: this is probably a consequence of a reduced formation rate of H_2 on to dust grains (probably because the gas is warm, $T > 1000$ K) and/or of an enhanced ionizing flux relative to what is observed in our Galaxy.

In this work, we present additional high signal-to-noise (S/N) ratio data on three of the DLAs in which H_2 is detected and the results of multicomponent Voigt profile fits to neutral and singly ionized species (including C I, C I* and C II*) in all the DLAs in our sample. We estimate the range of physical conditions in the neutral gas using standard techniques that are used in ISM studies. This paper is organized as follows. In Section 2, we give the details of the additional data and present the new fits to the H_2 absorption lines in the corresponding three systems. In Section 3, we discuss the relative populations of different H_2 rotational levels deriving information on the physical state of the gas by comparing the DLA observations with Galactic ISM, Small Magellanic Cloud (SMC) and Large Magellanic Cloud (LMC) data. In Sections 4 and 5, we discuss, respectively, the fine-structure excitation of C I and the ionization state of carbon. In Section 6, we study the C II* excitation in detail. Finally, we summarize our results and discuss various implications of the overall study in Section 7.

2 DATA SAMPLE

UVES (Dekker et al. 2000), installed at the European Southern Observatory Very Large Telescope (ESO VLT) 8.2-m telescope unit, Kueyen, on Mount Paranal in Chile was used to search for H_2 in a large sample of DLAs. The sample- and data-reduction procedures are described in detail in Ledoux et al. (2003). Observations and details of Voigt profile analysis of H_2 and metal line absorption lines towards Q 0013 − 004, Q 0551 − 366 and Q 1232 + 082, along the lines of sight of which H_2 is detected, are described in, respectively, Petitjean, Srianand & Ledoux (2002), Ledoux, Srianand & Petitjean (2002) and Srianand, Petitjean & Ledoux (2000). The Voigt profile fits to H_2 and other metal lines at $z_{\rm abs} = 3.024$ towards Q 0347 − 383, $z_{\rm abs} = 2.595$ towards Q 0405 − 443 and $z_{\rm abs} = 2.086\,8$ towards Q 1444 + 014 are discussed in Ledoux et al. (2003). For systems in which H_2 is not detected, Ledoux et al. (2003) have provided upper limits on $N(H_2)$ together with mean metallicities and depletion factors.

Recently, we have obtained additional higher spectral resolution spectra ($R \sim 55\,000$) of Q 0347 − 383 and Q 0405 − 443 as a part of our ongoing programme on cosmic variation of the electron-to-proton mass ratio (Petitjean et al. 2004). Nine exposures of 1.5 h each were taken for each of the quasars over six

nights under sub-arcsec seeing conditions in 2002 and 2003 January for Q 0347 − 383 and Q 0405 − 443, respectively. We have also obtained additional data of Q 1232 + 082 to study the HD lines that are detected in the DLA (Varshalovich et al. 2001). Spectra were reduced using the UVES pipeline, and addition of individual exposures was performed using a sliding window and weighting the signal by the errors in each pixel. We detect a new H_2 component at $z_{\rm abs} = 2.594\,86$ towards Q 0405 − 443 in addition to the strong component reported in Ledoux et al. (2003). We also present Voigt profile fits to the H_2 lines in the $z_{\rm abs} = 2.811$ system towards Q 0528 − 250. The single H_2 component seen in the lower spectral resolution Cassegrain Echelle Spectrograph (CASPEC) spectrum (Srianand & Petitjean 1998) is resolved into two distinct components in our new UVES spectra. For both these systems, the Voigt profile fits to the H_2 Lyman- and Werner-band absorption lines are shown in Fig. 1, and the resulting parameters are summarized in Table 1. This table also gives the results of Voigt profile fits to H_2 for the $z_{\rm abs} = 2.337\,72$ towards Q 1232+082.

The main purpose of this paper is to provide a detailed account of C I, C II* and other metal lines in DLAs of our sample and extract physical conditions in conjunction with the H_2 content reported in Ledoux et al. (2003). For the $z_{\rm abs} = 2.139$ system towards Tol 1037 + 014 and the $z_{\rm abs} = 3.350$ system towards Q 1117 − 1329, we use the results presented in Srianand & Petitjean (2001) and Péroux et al. (2002), respectively. For the rest of the systems, we give here the results of the multicomponent Voigt profile fits. For this,

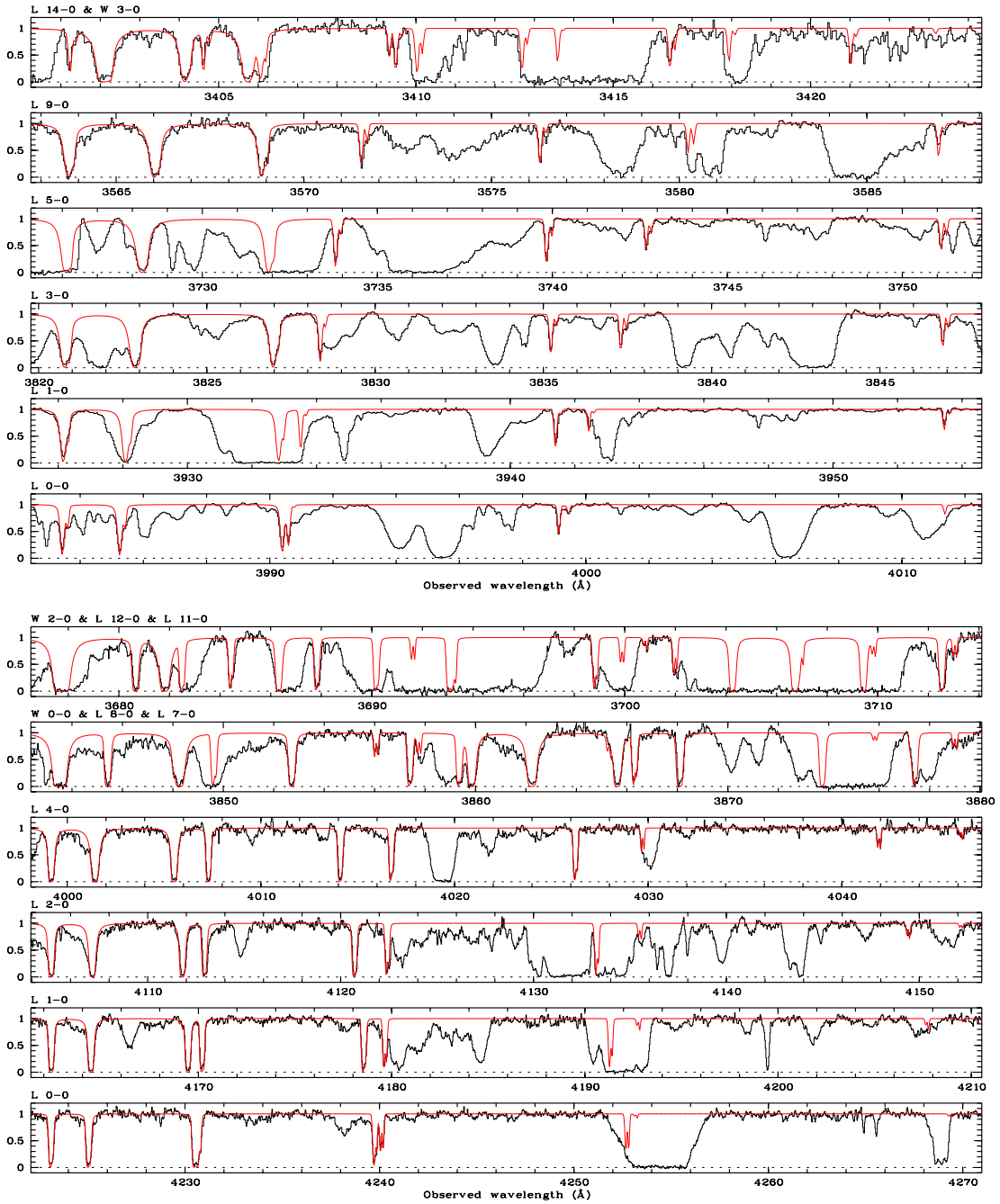

Figure 1. The Voigt profile fits to different rotational levels in the ground vibrational state of H_2 detected at $z_{\rm abs} = 2.594\,8$ towards Q 0405 − 443 (top panels) and $z_{\rm abs} = 2.811\,1$ towards Q 0528 − 250 (bottom panels). The fit parameters are given in Table 1.

Table 1. Results of Voigt profile fitting to H_2 absorption lines using the new data.

QSO	z_{abs}	J	log N (cm^{-2})	b (km s^{-1})
Q 0405 − 443	2.594 71	0	$17.65^{+0.07}_{-0.15}$	1.5 ± 0.5
		1	$17.97^{+0.05}_{-0.08}$	
		2	$15.93^{+0.75}_{-0.42}$	
		3	$14.81^{+0.14}_{-0.26}$	
		4	$\leqslant$13.55	
	2.594 86	0	$15.13^{+0.14}_{-0.10}$	1.1 ± 0.1
		1	$15.24^{+0.13}_{-0.02}$	
		2	$14.00^{+0.01}_{-0.11}$	
		3	$13.93^{+0.09}_{-0.05}$	
		4	$\leqslant$13.55	
Q 0528 − 250	2.811 00	0	$17.29^{+0.08}_{-0.16}$	2.8 ± 0.5
		1	$17.78^{+0.10}_{-0.15}$	
		2	$16.74^{+0.46}_{-0.46}$	
		3	$15.68^{+0.44}_{-0.17}$	
		4	$14.13^{+0.01}_{-0.01}$	
		5	$13.68^{+0.01}_{-0.01}$	
	2.811 12	0	$17.24^{+0.05}_{-0.01}$	1.0 ± 0.3
		1	$17.68^{+0.07}_{-0.04}$	
		2	$16.98^{+0.17}_{-0.36}$	
		3	$16.58^{+0.15}_{-0.59}$	
		4	$14.32^{+0.50}_{-0.15}$	
		5	$13.58^{+0.02}_{-0.04}$	
Q 1232 + 082	2.337 72	0	$19.34^{+0.10}_{-0.10}$	4.5 ± 0.5
		1	$19.17^{+0.10}_{-0.10}$	
		2	$16.70^{+0.22}_{-0.22}$	
		3	$16.90^{+0.32}_{-0.32}$	
		4	$14.68^{+0.05}_{-0.05}$	
		5	$14.45^{+0.04}_{-0.04}$	

we use a Voigt-profile fitting code that determines the best-fitting parameters (column density, velocity dispersion and redshift) using χ^2 minimization techniques (Chand et al. 2004). We use the oscillator strengths compiled in table 1 of Ledoux et al. (2003) for metal ions and those given by Morton & Dinerstein (1976) for H_2. In this article, we measure metallicities relative to solar, $[X/H] \equiv \log[N(X)/N(H)] - \log[N(X)/N(H)]_\odot$, with X = Zn, or S, or Si, and depletion factors of iron, $[X/Fe] \equiv \log[N(X)/N(Fe)] - \log[N(X)/N(Fe)]_\odot$, adopting the solar abundances from Savage & Sembach (1996).

3 DETERMINATION OF PHYSICAL PARAMETERS USING H_2 LEVEL POPULATION

In this section, we estimate different physical parameters from the column densities of H_2 in different J rotational levels.

3.1 Kinetic temperature of the gas

It is a standard procedure, in ISM studies, to use the ortho-to-para ratio (OPR) to infer the kinetic temperature of the gas assuming local thermodynamic equilibrium (LTE) (Tumlinson et al. 2002, and references therein). Indeed, recent numerical investigations suggest that the OPR is a good tracer of the kinetic temperature over large regions of the parameter space (Shaw et al. 2004). For completeness, we first review our understanding of the OPR and outline the method for deriving the kinetic temperature before applying the method to the data.

3.1.1 General outline

As the interconversion between para and ortho states involves a spin flip, it is not allowed for processes involving an isolated molecule (i.e. radiative processes cannot induce interconversion). Ortho/para interconversion is only possible through (i) spin exchange induced by collisions with protons (with a rate coefficient in the range 10^{-10} to 10^{-9} cm^3 s^{-1}; see Dalgarno, Black & Weisheit 1973; Flower & Watt 1984; Gerlich 1990) or with hydrogen atoms (with a rate coefficient, an order of magnitude less than that of protons; Mandy & Martin 1993; Tiné et al. 1997) and (ii) reactions on the surface of dust grains (Le Bourlot 2000). In the case of LTE,

$$\mathrm{OPR_{LTE}} = 3\frac{\sum_{J=\mathrm{odd}}(2J+1)\exp\left[-\mathrm{B}J(J+1)/T\right]}{\sum_{J=\mathrm{even}}(2J+1)\ \exp\left[-\mathrm{B}J(J+1)/T\right]}, \quad (1)$$

where J is the rotational quantum number, B is the rotational constant of H_2 (B = 85.3 K) and T is either the kinetic temperature of the gas (when OPR is governed by spin-exchange collisions) or the formation temperature (when OPR is governed by H_2 formation on the surface of dust grains with LTE distribution characterized by the formation temperature T_{form}; see Sternberg & Neufeld 1999; Takahashi 2001). The equilibrium temperature, T(OPR), can be obtained using the observed value of OPR and equation (1). This will trace the kinetic temperature of the gas if spin-exchange collisions are mainly responsible for the observed OPR.

If the gas is dense and cold and if most of the H_2 molecules are in the $J = 0$ and $J = 1$ levels, then

$$\mathrm{OPR_{LTE}} \sim \frac{N(J=1)}{N(J=0)} = 9\exp(-170.5/T_{01}). \quad (2)$$

In the case of optically very thick molecular gas for which there is enough self-shielding, the $N(J = 1)/N(J = 0)$ ratio can be maintained at its Boltzmann value and the excitation temperature, T_{01}, equals the kinetic temperature. Savage et al. (1977) measured the mean excitation temperature, $T_{01} = 77 \pm 17$ K, for the Galactic ISM. This is consistent with the mean temperature of the ISM measured using 21-cm absorption lines. Thus, it is widely believed that when there is sufficient shielding (i.e. $\log N(\mathrm{H_2})\,\mathrm{cm}^{-2} \geqslant 16.5$), T_{01} is a reasonably good tracer of the kinetic temperature. This is because in the shielded region, H_2 photodissociation time-scale can be larger than the time-scale for charge exchange collision (Flower & Watt 1984). Also, a recent multiwavelength study of Galactic sightlines shows the T_{01} measured in optically thick cases closely follows the spin temperature measured from 21-cm observations (see Roy, Chengalur & Srianand 2005).

The excitation temperature, T_{ij}, between different rotational levels (say $J = i$ and j) of a given species (either ortho or para H_2) can be obtained using

$$\frac{N(J=j)}{N(J=i)} = \frac{2j+1}{2i+1}\exp(-\mathrm{B}[j(j+1)-i(i+1)]/T_{ij}). \quad (3)$$

Unlike OPR, this ratio can be altered by radiation pumping and formation pumping in addition to collisions. If collisions dominate the rotational excitation, then T_{ij} will be equal to T(OPR). Presence of formation pumping and/or UV pumping will make $T_{ij} > T$(OPR).

Table 2. Excitation temperatures measured in individual H_2 components of DLAs in the sample of Ledoux et al. (2003).

QSO	z_{abs}	log N(H I)[a]	log $N(H_2)$	T_{01} (K)	T_{02} (K)	T_{13} (K)	OPR	T(OPR) (K)
Q 0013 − 004	1.966 85	20.83 (0.05)	$16.38^{+0.03}_{-0.04}$	300^{+276}_{-96}	766^{+584}_{-244}	395^{+59}_{-45}	1.85 ± 0.28	114^{+14}_{-12}
	1.968 22		$16.54^{+0.05}_{-0.05}$	73^{+7}_{-8}	302^{+33}_{-30}	519^{+59}_{-75}	0.64 ± 0.09	66^{+3}_{-4}
Q 0347 − 383	3.024 89	20.73 (0.05)	$14.55^{+0.09}_{-0.09}$	...	740^{+499}_{-212}	558^{+100}_{-73}	3.45 ± 0.47	$\geqslant 200$
Q 0405 − 443	2.594 71	21.05 (0.10)	$18.14^{+0.07}_{-0.12}$	121^{+10}_{-10}	101^{+24}_{-24}	104^{+4}_{-4}	2.10 ± 0.30	127^{+19}_{-15}
	2.594 86		$15.51^{+0.15}_{-0.07}$	91^{+6}_{-6}	118^{+5}_{-5}	219^{+19}_{-19}	1.34 ± 0.17	93^{+6}_{-7}
Q 0528 − 250	2.811 00	21.35 (0.07)	$17.93^{+0.14}_{-0.20}$	167^{+7}_{-7}	190^{+46}_{-46}	156^{+11}_{-11}	2.47 ± 0.36	152^{+50}_{-24}
	2.8111 2		$17.90^{+0.11}_{-0.14}$	138^{+12}_{-12}	238^{+46}_{-46}	278^{+57}_{-57}	1.83 ± 0.33	113^{+17}_{-13}
Q 0551 − 366	1.961 68	20.70 (0.08)	$15.64^{+0.40}_{-0.14}$	76^{+7}_{-7}	248^{+52}_{-52}	401^{+73}_{-73}	0.90 ± 0.16	76^{+8}_{-6}
	1.962 14		$17.40^{+0.65}_{-0.93}$	175^{+88}_{-88}	326^{+65}_{-65}	446^{+185}_{-185}	1.74 ± 0.72	108^{+42}_{-28}
	1.962 21		$15.58^{+0.03}_{-0.12}$	154^{+24}_{-24}	415^{+25}_{-25}	593^{+39}_{-39}	1.86 ± 0.23	115^{+13}_{-14}
Q 1232 + 082	2.337 72	20.90 (0.08)	$19.57^{+0.12}_{-0.12}$	67^{+12}_{-12}	67^{+6}_{-6}	148^{+22}_{-22}	0.73 ± 0.32	71^{+12}_{-16}
Q 1444 + 014	2.086 80	20.25 (0.07)	$16.49^{+0.28}_{-0.11}$	285^{+35}_{-35}	205^{+15}_{-15}	196^{+14}_{-14}	3.59 ± 0.42	$\geqslant 200$
	2.086 96		$18.15^{+0.15}_{-0.15}$	193^{+8}_{-8}	148^{+37}_{-37}	120^{+1}_{-1}	3.20 ± 0.28	$\geqslant 200$

Note. The $z_{abs} = 1.972\,96$ and 1.973 80 components towards Q 0013 − 004 are not considered here as the H_2 column densities of the $J = 0$ and $J = 1$ levels are not known accurately due to saturation effects (see Petitjean et al. 2002). [a]Integrated H I column density in all the components (with and without H_2).

In the following section we discuss various temperature estimates from the DLA sample.

3.1.2 *Kinetic temperature of the H_2 components*

In our sample, H_2 is only detected in $J \leqslant 5$ levels of the vibrational ground state. Thus, we compute the OPR by summing the H_2 column densities for levels with $J \leqslant 5$. The observed value of the OPR for each DLA is given in column 8 of Table 2. We calculate T(OPR) from the measured OPR for individual systems using equation (1) (see column 9 of Table 2). When the kinetic temperature (or formation temperature) is high (i.e. $T \geqslant 200$ K) the OPR reaches 3, the value expected based on spin statistics. For a kinetic temperature similar to that seen in the cold neutral medium (CNM) of our Galaxy ($\simeq$80 K), the expected OPR under LTE assumption is less than 1. From Table 2, it is clear that the LTE temperatures measured from the OPR for DLAs are most of the times higher than 80 K (the mean found in the Galactic ISM.)

In Fig. 2, we plot the observed values of the OPR against the total H_2 column density in the ISM (triangles), LMC (squares), SMC (asterisks) and DLAs (circles with error bars). It is apparent that most of the OPR values in DLAs are significantly different from three (see also column 8 of Table 2). The distribution of the OPR as a function of $N(H_2)$ in DLAs is consistent with that observed along Galaxy, LMC and SMC sightlines (see Fig. 2) when log $N(H_2) \leqslant 16$, and for the rest of the components, OPR in DLAs is systematically higher than that measured in the Galaxy, LMC and SMC. For example, OPR $\geqslant 3$ is seen only along sightlines with low H_2 optical depth (i.e. $N(H_2) \leqslant 10^{16}$ cm^{-2}) in the Galaxy, LMC and SMC (see Fig. 2). On the contrary, out of the three DLA components with OPR $\geqslant 3$, two, at $z_{abs} = 2.08\,680$ and $z_{abs} = 2.086\,92$ towards Q 1444 + 014, are optically thick in the Lyman-band absorption lines.

We next investigate the dependence of T_{01} (measured using equation 2) on the total H_2 column density (see Fig. 3). Individual values measured in DLAs are listed in Table 2 (see column 5). The large errors on both $N(H_2)$ and T_{01} are mostly a consequence of the difficulty to measure the Doppler parameter when the lines are saturated. In the case of the $z_{abs} = 1.966\,85$ component towards Q 0013 − 004, the uncertainty is a consequence of line blending (see Petitjean et al. 2002). The vertical dotted lines show the mean and 1σ range

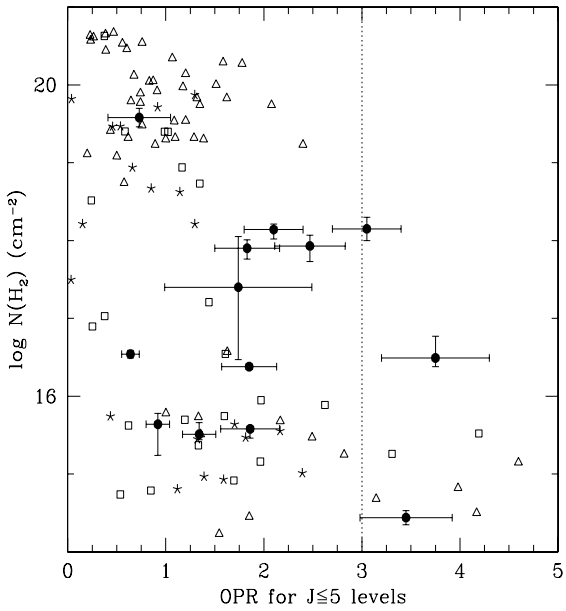

Figure 2. The OPR obtained using the populations of $J \leqslant 5$ rotational levels in individual components of DLAs (black dots) is plotted against the total H_2 column density. Other data points are from Savage et al. (1977), Spitzer, Cochran & Hirshfeld (1974) for the Galactic ISM (triangles) and Tumlinson et al. (2002) for the LMC (squares) and SMC (asterisks). The vertical short-dashed line shows the high-temperature LTE limit of the OPR (i.e. OPR = 3).

of T_{01} measured by Savage et al. (1977). The data points from the Magellanic Clouds (Tumlinson et al. 2002) are consistent with this range (mean $T_{01} = 82 \pm 21$ K). As in the case of the OPR, most of the measurements from DLAs with optically thick H_2 (i.e. log $N(H_2) \geqslant 16.5$) are well separated from that of the ISM and Magellanic Clouds (Fig. 3) and the spread seen in the optically thin case is consistent with that seen in local ISM. Note that the system with lowest molecular content ($z_{abs} = 3.024\,89$ towards 0347 − 383) has $N(J = 0)$, an order of magnitude lower than $N(J = 1)$. T_{01} cannot be computed in this case as the maximum expected column density

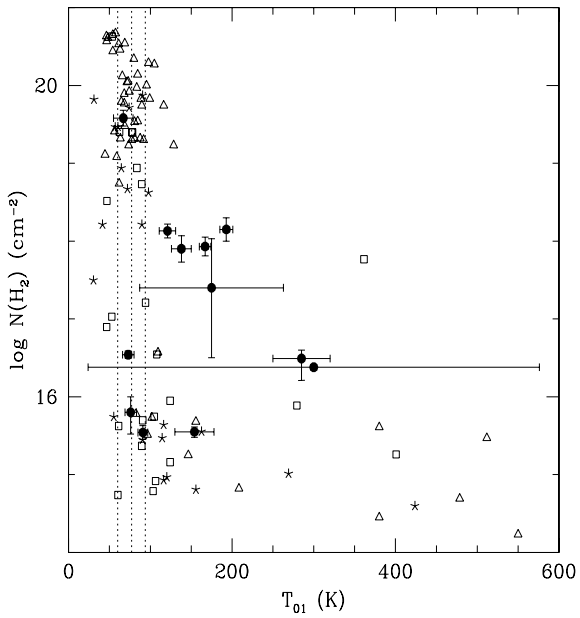

Figure 3. The rotational temperature T_{01} obtained from the $N(J=1)/N(J=0)$ ratio in DLAs (black dots) is plotted against the total column density of molecular hydrogen. Other data points are from Savage et al. (1977), Spitzer et al. (1974) for the Galactic ISM (triangles), and Tumlinson et al. (2002) for the LMC (squares) and SMC (asterisks). The vertical short-dashed lines show the mean and 1σ range of T_{01} measured by Savage et al. (1977) in the Galactic ISM.

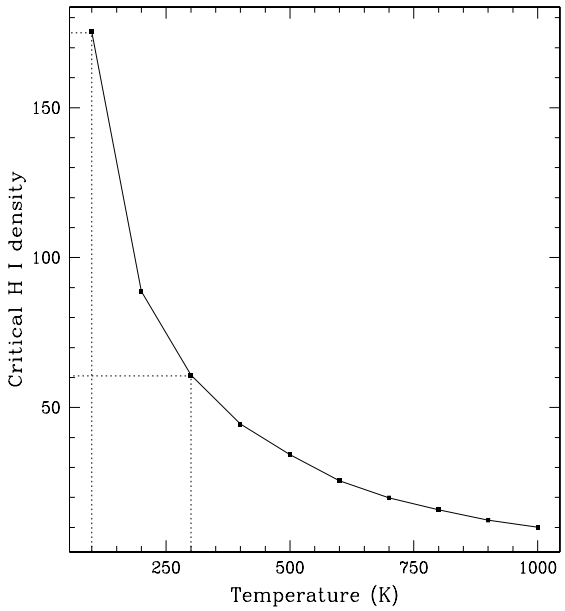

Figure 4. Critical hydrogen density ($n_{\rm H}$) as a function of kinetic temperature for the thermalization of the $J=0$ and 2 levels. The curve is obtained by equating the collisional de-excitation and spontaneous decay rates. We have used the collisional rates at low temperature given by Forrey et al. (1997). The spontaneous decay rates are from Turner, Kirby-Docken & Dalgarno (1977). It is clear from the short-dashed lines that for $100 \leqslant T \leqslant 300$ K the critical density is $175 \geqslant n_{\rm H}({\rm cm}^{-3}) \geqslant 60$.

ratio, $N(J=1)/N(J=2)$, is 9 under LTE conditions (see equation 2). For the high optical depth clouds (i.e. $\log N({\rm H_2})\,{\rm cm}^{-2} \geqslant 16.5$) in DLAs, the mean T_{01} is 153 ± 78 K. In most of the components, the two temperatures T_{01} and T(OPR) are consistent within errors. This is mainly because most of the H_2 molecules reside in the ground states.

In summary, if we assume LTE then T(OPR) and T_{01} measured in DLAs (with $\log N({\rm H_2}) \geqslant 16.5$) at high redshift are on an average higher than that measured in the ISM, LMC and SMC sightlines. In this high $N(H_2)$ range, T_{01} is expected to trace the kinetic temperature. However, in the case of optically thin systems the T(OPR) (or T_{01}) measured in DLAs are consistent with that measured in LMC, SMC and Galactic sightlines. Under the LTE assumption, we find that H_2 components in DLAs have kinetic temperatures in the range 100–200 K.

3.2 Rotational excitation

The rotational level populations are affected by particle collisions, UV pumping and formation pumping. While the collisional excitation plays a significant role in populating the low-J levels, those with $J \geqslant 3$ are usually populated by formation processes and UV pumping. In what follows, we discuss the excitation of H_2 as seen in DLAs and compare with ISM, LMC and SMC sightlines.

3.2.1 Low-J excitation

The collisional contribution to the excitation of H_2 can be investigated by studying the $N(J=2)/N(J=0)$ and $N(J=3)/N(J=1)$ ratios. In general, $J=2$ and $J=3$ levels can also be populated by the de-excitation of H_2 formed in the high-J states (usually referred to as formation pumping) or through UV pumping. The collisional excitation rate for the $J=0 \rightarrow 2$ transition is about an order of magnitude higher than that of the $J=1 \rightarrow 3$ transition for kinetic temperatures in the range 100–300 K (Forrey et al. 1997). The spontaneous decay rate from $J=3$ is an order of magnitude smaller than from $J=2$. This means that the ground and first excited states of para-H_2 can be thermalized at lower densities compared to that of ortho-H_2. In Fig. 4, we plot as a function of temperature, the critical hydrogen density for which the collisional de-excitation rate becomes equal to the spontaneous decay rate for the $J=2 \rightarrow J=0$ transition. It is clear from this figure that the hydrogen density has to be high (in the range 60–175 cm^{-3}) in order for the $N(J=2)/N(J=0)$ ratio to be equal to the LTE value corresponding to typical kinetic temperatures inferred from the OPR (i.e. 100–300 K).

In Fig. 5, we plot the ratio, $N(J=2)/N(J=0)$, observed in DLAs, the Galaxy, LMC and SMC as a function of the total H_2 column density. The vertical dotted lines in the figure show the expected values of the ratio for four different excitation temperatures assuming LTE. The values of the excitation temperature T_{02} for individual DLA H_2 components obtained using equation (3) are given in Table 2. The observed excitation temperatures are in the range 100–600 K with most of them at $T_{02} \simeq$ 150–300 K. If the level populations are in LTE, then the required hydrogen density to maintain the equilibrium is 65–150 cm^{-3} (see Fig. 4). We can see from Fig. 5 that in DLAs where H_2 is optically thick, the $N(J=2)/N(J=0)$ ratio is larger than that seen in similar gas of the Galactic ISM, LMC and SMC. It can be seen from Table 2 that, in most of the DLAs, T_{01} is lower than or equal to T_{02} (see Table 2). This is very much the case as well in most of the sightlines through the ISM and Magellanic Clouds. It is well known that, due to a lower value of the Einstein coefficient of the $J=2$ level compared to those of higher J levels, the UV and formation pumping processes

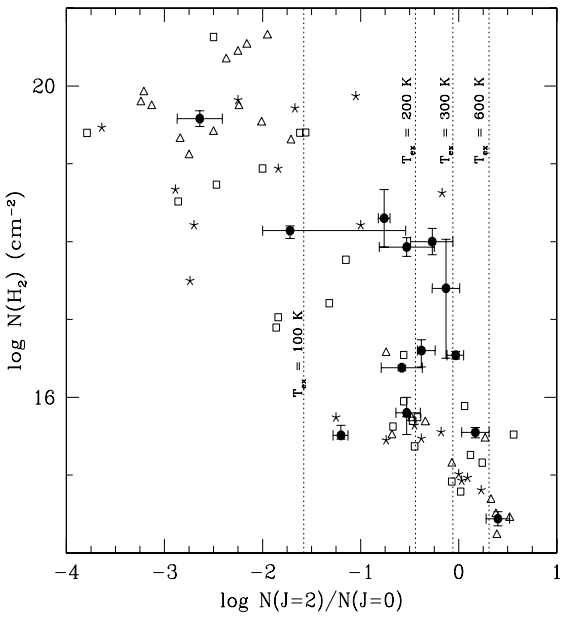

Figure 5. The $N(J = 2)/N(J = 0)$ ratio observed in individual DLA components (black dots) is plotted against the total molecular hydrogen column density. Other data points are from Savage et al. (1977), Spitzer et al. (1974) for the Galactic ISM (triangles), and Tumlinson et al. (2002) for the LMC (squares) and SMC (asterisks). The vertical dotted lines are the expected values of the column density ratio assuming the LTE for four different excitation temperatures.

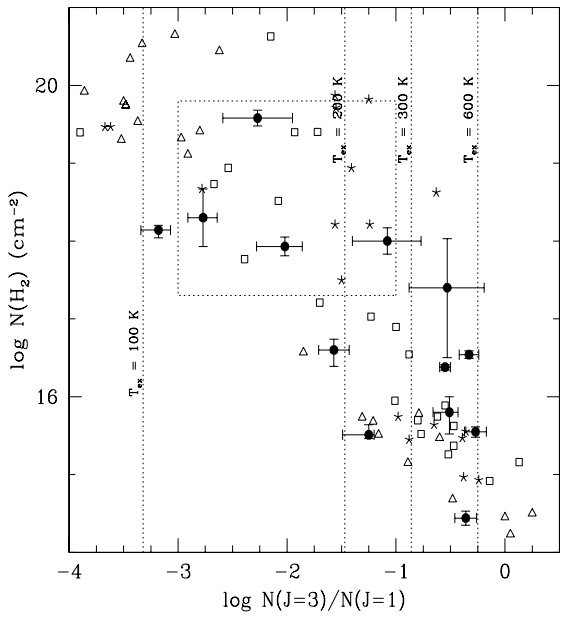

Figure 6. The $N(J = 3)/N(J = 1)$ ratio observed in individual DLA components (black dots) is plotted against the total molecular hydrogen column density. The box drawn with dotted lines gives the allowed range for the $z_{\rm abs} = 1.973$ components towards Q 0013 − 004. Other data points are from Savage et al. (1977), Spitzer et al. (1974) for the Galactic ISM (triangles), and Tumlinson et al. (2002) for the LMC (squares) and SMC (asterisks). The vertical dotted lines are the expected values of the column density ratio assuming the LTE for four different excitation temperatures.

can lead to enhancing the $J = 2$ level compared to the $J = 0$ level. Thus, the higher values of $N(J = 2)/N(J = 0)$ seen in DLAs can be explained by higher pressure in the gas and/or higher radiation field.

Fig. 6 gives the $N(J = 3)/N(J = 1)$ ratio as a function of $N(H_2)$. The vertical dotted lines in the figure show the expected value of the ratio for four different excitation temperatures under the LTE assumption. The measurements in DLAs are consistent with local measurements, and the excitation temperature T_{03} is in the range 100 − 680 K (see Table 2). In Fig. 7, we plot the $N(J = 3)/N(J = 1)$ ratio versus the $N(J = 2)/N(J = 0)$ ratio. If formation and UV pumping contribute appreciably to populate the $J = 2$ and $J = 3$ levels then we expect a tight relationship between the two quantities. The dotted line in the figure gives the expected relationship between the ratios under LTE. In the case of sightlines through the Galactic ISM, the LMC or SMC, the $N(J = 3)/N(J = 1)$ ratio is higher than what is expected from the $N(J = 2)/N(J = 0)$ value under LTE (or, T_{13} is higher than T_{02}). In the case of DLAs, most of the components have T_{13} close to T_{02} (points are on top of the dotted line). Note that these excitation temperatures are different from T_{01}. This clearly means that UV pumping and formation pumping are not negligible even for the excitation of the low J levels. The nature of the local radiation field can be probed using excitations of $J \geqslant 3$ levels. This is what we do in the following section.

3.2.2 UV radiation field: high-J excitation

It is known that in the photodissociation regions (PDRs) the $J = 4$ and $J = 5$ rotational levels are populated predominantly by cascades following the formation of excited molecules and UV pumping from the low-J states. As radiative decay time-scales for these levels are very short compared to the collisional time-scales, spontaneous decay is the main deexitation process. Among the two populating processes, the UV pumping is an optical depth-dependent process while the formation pumping is independent of optical depth. In an optically thick cloud, UV pumping is efficient in a thin shell surrounding the cloud. In the interior of the cloud, UV pumping becomes important only when the column density becomes very large (i.e. through absorption in the damping wings).

In Fig. 8, we plot $\log N(H_2)$ as a function of $\log N(J = 4)/N(J = 0)$ as measured in DLAs and along the ISM, LMC and SMC sightlines. As expected, a strong anticorrelation is present in the data, including DLAs. H_2 absorption lines in DLAs have no strong overlapping wings. Therefore, the high-J excitation is mostly due to photoabsorption in the systems with $\log N(H_2) \leqslant 16.5$ and to H_2 formation in the systems with higher column densities. Following analytic prescription by Jura (1975), we can write

$$p_{4,0}\beta(0)n(H_2, J = 0) + 0.24Rn(H)n = A(4 \rightarrow 2)n(H_2, J = 4). \quad (4)$$

Here, $\beta(0)$ and $p_{4,0}$ are, respectively, the photoabsorption rate in the Lyman and Werner bands and the pumping efficiency from $J = 0$ to $J = 4$; A(4 → 2) is the spontaneous transition probability between $J = 4$ and $J = 2$ and R is the formation rate of H_2. Neglecting the second term in the left-hand side of equation (4) leads to a conservative upper limit on the UV radiation field. The vertical dashed lines in Fig. 8 represent the corresponding predicted values of the $N(J = 4)/N(J = 1)$ ratio for $\beta(0) = 2 \times 10^{-10}\,s^{-1}$ (i.e., approximatively the mean radiation field in the ISM) and $\beta(0) = 2 \times 10^{-9}\,s^{-1}$. It can be seen from Fig. 8 that for $\log N(H_2)$ less than 16.5 the $N(J = 4)/N(J = 0)$ ratio in DLAs is of the order of or slightly higher than that seen in the ISM of our Galaxy. Quantitatively, the

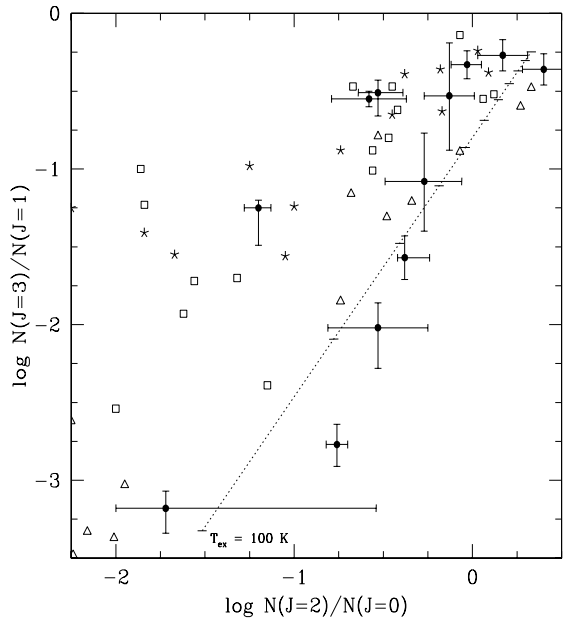

Figure 7. The $N(J=3)/N(J=1)$ versus $N(J=2)/N(J=0)$. DLA measurements are indicated by black dots. Other data points are from Savage et al. (1977), Spitzer et al. (1974) for the Galactic ISM (triangles), and Tumlinson et al. (2002) for the LMC (squares) and SMC (asterisks). The dotted line gives the expected relation under LTE with temperatures ranging from 100 to 600 K (horizontal tick-marks show the values for different temperatures with 50-K steps).

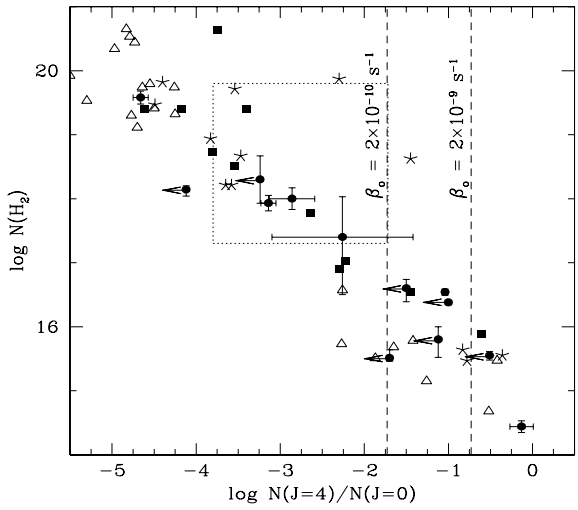

Figure 8. The $N(J=4)/N(J=0)$ ratio is plotted against the total molecular hydrogen column density. DLA measurements are indicated by black dots. Other data points are from Savage et al. (1977), Spitzer et al. (1974) for the Galactic ISM (triangles), and Tumlinson et al. (2002) for the LMC (squares) and SMC (asterisks). The box with dotted lines gives the allowed range for the $z_{\rm abs} = 1.973$ component towards Q 0013 − 004. The vertical dashed lines are the expected values of the ratio for two different values of the photoabsorption rate (β_0).

upper limits in most of the systems are consistent with $2 \times 10^{-10} \leqslant \beta(0) \leqslant 2 \times 10^{-9}\,{\rm s}^{-1}$. This probably means the optically thin H_2 components without detectable H_2 absorption lines from the $J=4$ state arise in gas embedded in an UV field with intensity similar to (or slightly higher than) that of the mean ISM field.

There are two optically thin components in our sample ($z_{\rm abs} = 1.968\,22$ towards Q 0013 − 004 and $z_{\rm abs} = 3.024\,89$ towards Q 0347 − 383), which show detectable $J=4$ H_2 absorption lines. Detailed analysis of these components suggests an ambient field intensity consistent with few times the mean ISM field intensity (Levshakov et al. 2002; Petitjean et al. 2002). The same conclusion was derived by Reimers et al. (2003) for the optically thin H_2 component at $z_{\rm abs} = 1.15$ system towards HE 0515 − 4414.

The above ratio has similar values at high $\log N(H_2)$ in DLAs and in our Galaxy. This is a hint for the formation pumping in DLAs with high $N(H_2)$ being similar to the local one. There are two optically thick components (at $z_{\rm abs} = 2.594\,71$ towards Q 0405 − 443 and $z_{\rm abs} = 2.086\,96$ towards Q 1444 + 014) that do not show detectable absorption lines from $J=4$ state. In the latter system, the ratio $N(J=4)/N(J=0) \leqslant 10^{-4}$. This is much lower than the values seen in the ISM at similar total $N(H_2)$ and could be a consequence of lower H_2 formation rate in this system. High values of the radiation field intensity were inferred for some of the optically thick components when the contribution of the second term in equation (4) is estimated using the average metallicity and dust depletion (Ge & Bechtold 1997; Petitjean, Srianand & Ledoux 2000; Ge, Bechtold & Kulkarni 2001).

4 ANALYSIS OF CARBON ABSORPTION LINES

As the ionization potential of C I is 11.2 eV, the ionization state of carbon is sensitive to the same photons that destroy H_2. Therefore, C I is usually a good tracer of the physical conditions in the molecular gas (see, however, Srianand & Petitjean 1998). In what follows, we investigate the relationship between the detectability of C I absorption line and other measurable quantities in our spectra. We derive additional constraints on the physical conditions in DLAs using C I fine-structure absorption lines.

4.1 Detectability of C I absorption lines

The results of simultaneous Voigt profile fitting to C I, C I* and C I** absorption lines in our sample are summarized in Table 3.

In the ISM of our Galaxy, all clouds with $\log N({\rm H\,I}) \geqslant 21$ have $\log N(H_2) > 19$ and $\log N({\rm C\,I}) > 14$ (Jenkins & Shaya 1979; Jenkins, Jura & Loewenstein 1983). In our sample, C I absorption lines are detected in most of the DLAs that show H_2 absorption lines (see also Ge & Bechtold 1999). There are three exceptions: the components at $z_{\rm abs} = 2.594\,71$ and $2.594\,86$ towards Q 0405 − 443 and at $z_{\rm abs} = 2.811\,00$ towards PKS 0528 − 250. These C I non-detections are surprising as the H_2 absorption lines from these components are optically thick so that C I is expected to be conspicuous.

Usually, DLAs in which no H_2 is detected through the whole profile do not show any detectable C I absorption line (with a typical upper limit of $10^{12}\,{\rm cm}^{-2}$). The only exception is the high-metallicity sub-DLA at $z_{\rm abs} = 2.139$ towards Tol 1037 − 270 (see Srianand & Petitjean 2001). On the contrary, in DLAs where H_2 is detected, some components show detectable C I absorption line without detectable molecular absorption ($N(H_2) \leqslant 10^{14}\,{\rm cm}^{-2}$). This is the case in Q 0013 − 004 (Petitjean et al. 2002) and Q 0551 − 366 (Ledoux et al. 2002).

Note that C I is also detected at $z_{\rm abs} = 2.287\,49$ towards Q 2332 − 094, but the presence of H_2 molecules cannot be probed in this system due to the presence of an intervening Lyman limit system. The sub-DLA at $z = 1.15$ towards HE 0515 − 4414 shows C I and H_2 absorption lines (Quast, Baade & Reimers 2002; Reimers

Table 3. DLA systems with detected C I absorption lines in the sample of Ledoux et al. (2003).

Quasar/ log N (H I)	z_{abs}	log $N(H_2)$	log N(C I)	log N(C I*)	log N(C I**)	b (km s^{-1})	T_{CMB}(K)	n_H(cm^{-3})	p/K (cm^{-3} K)
Q 0013−004	1.966 79	[a]$16.38^{+0.03}_{-0.04}$	13.06 ± 0.04	12.72 ± 0.05	....	3.1 ± 0.6	<13.8	20 − 70	2000 − 7000
20.83(0.05)	1.966 91	....	12.86 ± 0.03	12.55 ± 0.07	....	3.0 ± 0.2	<14.5	20 − 80	2000 − 8000
	1.967 06	....	12.31 ± 0.07	12.26 ± 0.11	....	4.93 ± 1.44	....	....	....
	1.968 22	$16.54^{+0.05}_{-0.05}$	13.04 ± 0.01	13.10 ± 0.01	12.77 ± 0.02	4.3 ± 0.2	<20.0	170 − 200	11730 − 12400
	1.972 80	[b]17.48−19.78	13.08 ± 0.01	12.77 ± 0.03	....	6.0 ± 0.3	<13.0	40 − 60	4000 − 6000
	1.972 96		13.44 ± 0.01	13.20 ± 0.01	12.53 ± 0.04	6.2 ± 0.2	<13.5	50 − 65	5000 − 6500
	1.973 16		12.66 ± 0.03	12.33 ± 0.10	....	7.0 ± 0.8	<15.0	10 − 85	1000 − 8500
	1.973 65	[c]17.30−19.60	12.32 ± 0.05	<12.11	....	5.7 ± 0.4	<15.0	<85	<8500
	1.973 82	....	12.40 ± 0.04	12.04 ± 0.13	....	4.5 ± 0.4	<15.5	<95	<9500
	1.973 99	....	11.91 ± 0.13	....	....	7.3 ± 1.0	....	....	....
	1.974 17	....	11.49 ± 0.25	....	....	0.4 ± 0.3	....	....	....
	1.967 37	<14.0	12.91 ± 0.03	12.77 ± 0.06	....	14.4 ± 1.1	<17.5	40 − 135	4000 − 13500
	1.967 63	<14.0	12.85 ± 0.05	12.68 ± 0.09	....	27.1 ± 3.4	<19.3	20 − 180	2000 − 18000
	1.971 09	<14.0	12.28 ± 0.03	<12.11	....	10.0 ± 0.9	<21.0	<200	<20000
	1.971 44	<14.0	12.96 ± 0.03	12.91 ± 0.03	....	13.4 ± 0.9	<18.5	65 − 160	6500 − 16000
Q 0347−383	3.024 85	$14.55^{+0.09}_{-0.09}$	11.73 ± 0.26	<11.50	<11.75	4.9 ± 0.3	<17.0	<48	<4800
20.73(0.05)									
Q 0405−443	2.594 74	$18.14^{+0.07}_{-0.12}$	<12.23	....	....	....	....	....	....
21.05(0.10)	2.594 85	$15.51^{+0.15}_{-0.07}$	<11.90	....	....	....	....	....	....
Q 0528−250	2.811 00	$17.93^{+0.14}_{-0.20}$	<12.00	....	....	....	....	....	....
21.35(0.10)	2.811 12	$17.90^{+0.11}_{-0.14}$	12.36 ± 0.10	12.30 ± 0.10	.....	0.6 ± 0.1	<17.0	25 − 270	3250 − 17000
Q 0551−366	1.961 52	<14.0	12.69 ± 0.07	<12.18	<11.94	4.3 ± 1.4	<10.5	<17	<1700
20.70(0.10)	1.961 68	$15.80^{+0.40}_{-0.14}$	12.64 ± 0.07	12.84 ± 0.07	<12.16	2.1 ± 0.7	<22.3	170 − 185	12950 − 14280
	1.961 80	<14.0	12.42 ± 0.13	<12.18	<11.94	3.9 ± 2.3	<12.9	<56	<5600
	1.962 14	$17.40^{+0.65}_{-0.93}$	12.66 ± 0.12	12.69 ± 0.11	12.11 ± 0.34	2.1 ± 0.8	<18.7	55 − 390	8250 − 30400
	1.962 21	$15.58^{+0.03}_{-0.12}$	13.16 ± 0.06	12.98 ± 0.09	12.26 ± 0.36	12.8 ± 1.7	<14.5	30 − 150	3840 − 15150
	1.962 68	<14.0	12.63 ± 0.08	<12.18	<11.94	4.0 ± 1.8	<10.0	<25	<2500
Q 1037−270	2.139 00	<14.0	12.51 ± 0.02	<12.48	....	15.5 ± 0.6	<16.4	<105	<10500
19.70(0.05)	2.139 40	<14.0	12.48 ± 0.02	<12.30	....	4.5 ± 1.2	<13.2	<65	<6500
Q 1232 + 082	2.337 71	$19.57^{+0.12}_{-0.12}$	13.86 ± 0.22	13.43 ± 0.07	12.63 ± 0.22	1.7 ± 0.1	<14	40 − 60	2320 − 5280
20.90(0.08)									
Q 1444 + 014	2.08679	$16.60^{+0.28}_{-0.11}$	12.67 ± 0.09	12.52 ± 0.14	....	11.6 ± 2.8	<18.5	20 − 110	6560 − 27280
20.25(0.07)	2.086 92	$18.15^{+0.15}_{-0.15}$	12.82 ± 0.11	12.42 ± 0.12	....	1.1 ± 0.3	<14.0	4 − 54	824 − 10260
Q 2332−094	2.287 49	....	13.33 ± 0.03	13.14 ± 0.03	12.34 ± 0.11	3.8 ± 0.3	<14.6	45 − 75	4500 − 7500
20.25(0.07)									

Note. [a]Total H_2 column density in three components at $z_{abs} = 1.966\,79$, 1.966 91 and 1.967 06 is quoted. [b]Total H_2 column density in three components at $z_{abs} = 1.972\,80$, 1.972 96 and 1.973 16. [c]Total H_2 column density in four components at $z_{abs} = 1.973\,65$, 1.973 82, 1.973 99 and 1.974 17 is quoted.

et al. 2003). C I absorption lines have also been detected at $z_{abs} = 1.776$ system towards Q 1331 + 170 (Chaffee, Foltz & Black 1988). The presence of H_2 in this system is recently reported (Cui et al. 2004).

4.1.1 *Dependence on H_2 column density*

Jenkins & Shaya (1979) found N(C I) does not scale linearly with N(H I), $N(H_2)$, or $N(H_{total})$ in the Galactic ISM. They explained this behaviour as a result of strong differences in the response of C I, H I and H_2 to physical conditions (electron density, temperature, etc.), coupled with marked variations of these conditions from one cloud to the other. In Fig. 9, we plot the C I column density as a function of H_2 column density in individual components. Among the systems that show H_2 absorption lines (filled circles with error bars), there is no clear trend between $N(H_2)$ and N(C I) even though the presence of C I absorption lines usually indicates the presence of H_2 (see discussion above).

4.1.2 *The carbon ionization state*

The probability of detecting C I is expected to be higher in systems with higher N(H I) and/or metallicity. Ideally, we would like, therefore, to know N(H I) for each individual C I component. This is not possible as all components are definitely blended in one strong H I DLA absorption line. Estimation of N(H I) is possible when the H_2 component is well separated from the rest of the components (as in $z_{abs} = 1.968\,22$ towards Q 0013 − 004) or when 21-cm observations are available (as in the case of H_2 components towards Q 0528 − 250). Note that the presence of very strong C I absorption line in the component at $z_{abs} = 1.968\,22$ towards Q 0013 − 004 (that has

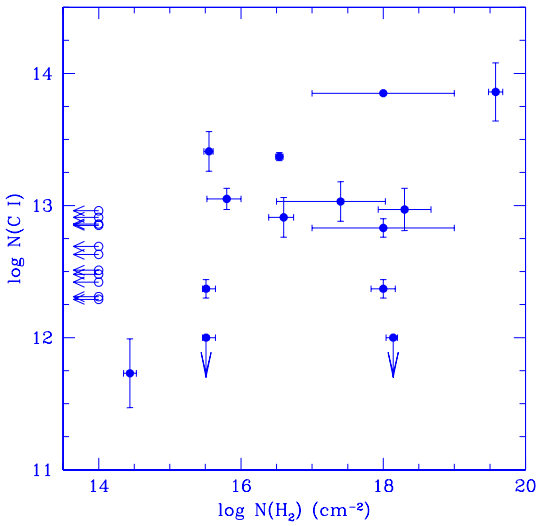

Figure 9. The column density of C I measured in individual components of DLAs is plotted as a function of $N(H_2)$. The filled circles with error bars are points from the components that show detectable H_2 absorption lines. The open circles are the measurements from components that show C I without detectable H_2.

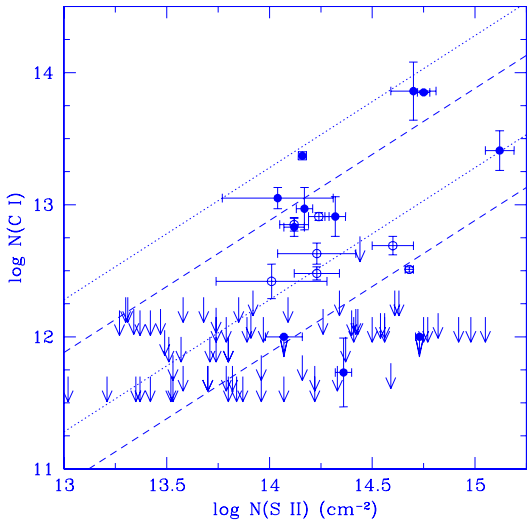

Figure 10. The C I column density measured in individual components of DLAs is plotted as a function of the S II column density. The filled circles with error bars are points from components that show detectable H_2 absorption lines. The open circles are the measurements from components that show C I but no detectable H_2. The arrows are the upper limits from systems where there is no H_2 and/or C I absorption lines. The two dotted lines give the expected correlation for $\log N(\mathrm{C\,I})/N(\mathrm{C\,II}) = -3$ (lower line) and -2 (upper line), respectively, when solar relative abundances are used and it is assumed that there is no depletion of carbon relative to sulphur. The short-dashed lines give the same correlations when a depletion of carbon relative to sulphur of 0.4 dex is further assumed. The C I detections are consistent with what one expects in the case of the CNM.

log$N$(H I) $\leqslant$ 19.4) is mainly due to high metallicity (Petitjean et al. 2002). Whereas, the absence of C I in the component at $z_{\rm abs} = 2.811\,00$ and the weakness of C I line of the component at $z_{\rm abs} = 2.811\,12$ component towards Q 0528 − 250 are probably due to excess radiation field from the QSO.

The ionization state of carbon is difficult to determine as the C IIλ1334 absorption line is usually highly saturated. We can, however, partly overcome this difficulty assuming that conditions are fairly homogeneous in the DLAs. Under the assumptions that the enrichment of carbon follows that of α-elements and that the relative depletion between sulphur and carbon is negligible, we can use the well-determined N(S II) as an indicator of N (C II) (see Fig. 10). In the Sun, the carbon abundance is 1.28 dex higher than that of sulphur and typical depletion of carbon relative to sulphur in the cold ISM is 0.4 dex (see table 5 of Welty et al. 1999). The two dotted lines in Fig. 10 give the expected correlation for $\log N(\mathrm{C\,I})/N(\mathrm{C\,II}) = -3$ (lower line) and -2 (upper line), respectively, when relative solar abundances are used and it is assumed that there is no depletion of carbon relative to sulphur. The short-dashed lines give the same correlations when a depletion of carbon relative to sulphur of 0.4 dex is further assumed. If the absorbing gas originates from the CNM then $\log N(\mathrm{C\,I})/N(\mathrm{C\,II})$ is expected to be more than -3 (see Fig. 3 of Liszt 2002). Therefore, within uncertainties due to depletion, it is apparent from Fig. 10 that the DLA components with C I detections have an ionization state consistent with them originating from the CNM.

It is interesting to note that the distribution of N(S II) is somewhat similar for components with both H_2 and C I absorption lines (filled circles), and for components with C I but no H_2 absorption lines (open circles). However, C I column densities are typically lower in the components without H_2 suggesting, as expected, that when H_2 is seen, the C I/C II ratio is larger.

Most of the upper limits on C I are consistent with $N(\mathrm{C\,I})/N(\mathrm{C\,II}) \leqslant -3$ (see Fig. 10). This can mean either that the relative depletion of carbon compared to sulphur is larger than 0.4 dex in the CNM, which is unlikely, or that most of the DLA systems originate from the warm neutral medium (WNM) or warm ionized medium (WIM) where the above ratio can be as low as 10^{-4}.

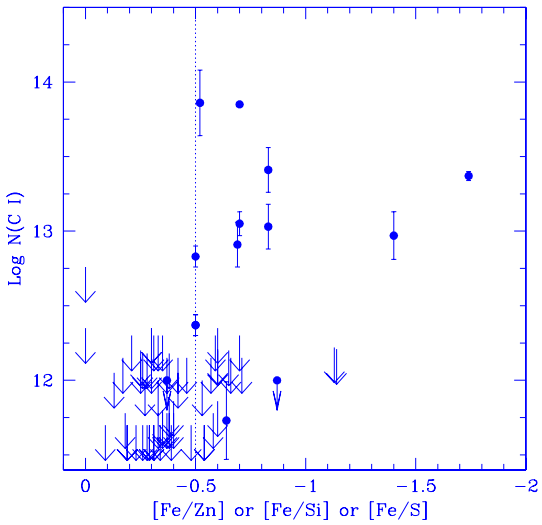

Figure 11. The column density of C I measured in individual components is plotted as a function of the metal depletion factor computed using [Fe/Zn] or [Fe/S] or [Fe/Si]. It is apparent from this figure that C I absorption line is usually detected in components with high depletion factors.

4.1.3 The effect of dust

In Fig. 11, we plot log N(C I) against the depletion factor defined as log $(N(\mathrm{Fe\,II})/N(\mathrm{X\,II}))-[\mathrm{Fe/X}]_\odot$ with either X = Zn or S or

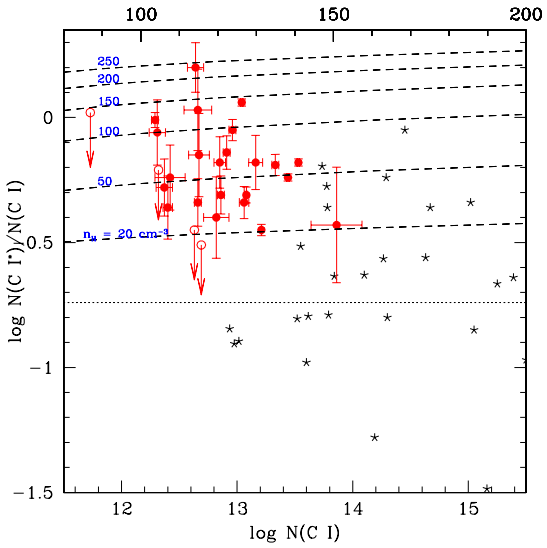

Figure 12. The ratio $N(\mathrm{C\,I^*})/N(\mathrm{C\,I})$ is plotted on a logarithmic scale as a function of $N(\mathrm{C\,I})$. The points with error bars are our measurements in individual DLA components. The stars are data measurements in the ISM of the galaxy drawn from Jenkins & Tripp (2001) and Jenkins et al. (1983). The horizontal dotted line gives the expected value of the ratio if it is assumed that C I is excited by the CMBR only with $T_{\mathrm{CMBR}} = 8.1$ K as expected at $z = 2$. The short dashed lines give the expected ratio for different n_{H} as a function of temperature (top portion of the x-axis).

Si. C I absorption line is not detected in systems with low depletion factors (i.e. [Fe/Zn] less than −0.5 dex) whereas, components with higher depletion factors readily show detectable C I absorption lines. This trend is not surprising as there is a 4σ correlation between the depletion factor and the metallicity of the gas in our sample (see Fig. 12 of Ledoux et al. 2003). Depletion factors lower than 0.5 dex are usually seen in systems with [Zn/H] $\leqslant -1$. High depletion factor in high metallicity gas implies high dust content and, hence, high dust optical depth to the UV radiation. The absence of C I in components with low dust depletion is a combination of low metallicity and low dust optical depth to the UV radiation. It is worth remembering that similar relation exists between the detectability of H_2 and depletion (fig. 14 of Ledoux et al. 2003).

4.2 C I fine-structure excitation

In most of the DLAs with C I detections, we also detect absorption lines from the excited fine-structure levels. It is therefore possible to use the relative populations of the C I ground state levels to discuss the particle density, the ambient UV radiation field and the temperature of the cosmic microwave background radiation (see Bahcall, Joss & Lynds 1973; Meyer et al. 1986; Songaila et al. 1994; Ge, Bechtold & Black 1997; Roth & Bauer 1999; Srianand et al. 2000; Silva & Viegas 2002; Quast et al. 2002). In the Galactic ISM, fine-structure excitation of C I has been used to study the distribution of thermal pressure (see Jenkins & Tripp 2001).

In Fig. 12, we plot the ratio $N(\mathrm{C\,I^*})/N(\mathrm{C\,I})$ as a function of $N(\mathrm{C\,I})$. It is clear that the C I column densities in DLAs (filled circles with error bars) are at least an order of magnitude less than that measured in the ISM (stars). This is probably a consequence of lower metallicities and/or low H I content in DLA components. The important point is that the $N(\mathrm{C\,I^*})/N(\mathrm{C\,I})$ ratio measured in DLAs is remarkably larger than in the Galaxy. However, while comparing the ISM and DLAs, it is important to remember that most of the sightlines used by Jenkins & Tripp (2001) have H_2 fraction orders of magnitude higher than what we measure in DLA components. As H_2 collisions are less efficient in populating the excited fine-structure state of C I, we expect that for a given total hydrogen density (and a given kinetic temperature), $N(\mathrm{C\,I^*})/N(\mathrm{C\,I})$ be higher in DLAs.

The horizontal dotted line in Fig. 12 indicates the expected value of the ratio if it is assumed that the excitation is due to the cosmic microwave background radiation (CMBR) only with a temperature $T_{\mathrm{CMBR}} = 8.1$ K as expected at $z = 2$, the typical redshift of our sample. It is clear that the CMBR field expected from the big bang is not sufficient to explain the observed ratios, and an extra contribution is required from collisional processes and/or the UV flux.

Collisions with H, He, e, p and H_2 can populate the excited state of C I. As H I is the dominant form of hydrogen in the gas, the contribution to the fine-structure excitation by H_2 collisions can be neglected. The electron and proton densities are expected to be very small, at least smaller by two orders of magnitude than the hydrogen density, and their contribution is also negligible (Keenan et al. 1986). The He I collisional rates are much less than that of H I, and the He I/H I ratio is small, which makes collisions with He I unimportant (see fig. 1 of Silva & Viegas 2002). Thus, in our analysis of the C I excitation, we consider only collisions by neutral hydrogen. The rates are taken from Launay & Roueff (1977). The spontaneous decay rates are $A_{10} = 7.93 \times 10^{-8}\,\mathrm{s^{-1}}$ and $A_{21} = 2.68 \times 10^{-7}\,\mathrm{s^{-1}}$ (Bahcall & Wolf 1968). The corresponding CMBR excitation rate is derived from these values. The UV pumping rate in the cloud depends on the nature and strength of the UV radiation field. We assume that the UV intensity is the same as in the ISM of our Galaxy as suggested by the high-J excitation of H_2.

The dashed lines in Fig. 12 give the expected ratio for, $T_{\mathrm{CMBR}} = 8$ K, an UV radiation field like in the Galaxy (with an excitation rate of $\Gamma_{01} = 7.55 \times 10^{-10}\,\mathrm{s^{-1}}$), hydrogen density in the range $n_{\mathrm{H}} = 20$–$250\,\mathrm{cm^{-3}}$, versus the kinetic temperature, T_{kin}, in the range 80–200 K (consistent with T_{01} measured in DLAs). It can be seen that a typical density range consistent with most of the observed point is $20 \leqslant n_{\mathrm{H}}\,(\mathrm{cm^{-3}}) \leqslant 150$. The density ($n_{\mathrm{H}}$) and pressure ($p/K$) derived for individual components are summarized in column 9 and 10, respectively, in Table 3. Here, we assume $T_{\mathrm{CMBR}} = 2.7 \times (1 + z_{\mathrm{abs}})$ and $T = T_{01}$ in the case of H_2 detection and $T = 100$ K otherwise. The derived pressure range in DLA components is higher than that typically measured in the Galactic ISM (see Jenkins & Tripp 2001) and consistent with what is expected in the CNM with lower metallicity ($Z \sim 0.1\,Z_{\odot}$) and dust depletion (see Wolfire et al. 1995, 2003; Wolfe et al. 2003a,b; Srianand et al. 2005). Interestingly, the derived density range in most of the components is close to the critical density for thermalizing the H_2 $N(J = 2)/N(J = 0)$ ratio (see Fig. 4).

5 CARBON IONIZATION STATE

In the ISM, when hydrogen is neutral, most of the carbon is in the form of C II so that we can use the C I/C II ratio to derive the physical conditions in the gas. As already mentioned, the C II absorption features are always badly saturated, and we rely on the realistic assumption that C II in the neutral phase can be traced by S II and/or Si II so that we can use the weak lines of these species to derive the C II column densities in the components of interest.

Assuming photoionization equilibrium between C I and C II and using the atomic data from Shull & van Steenberg (1982) and

Table 4. Physical conditions in systems in which C I is detected.

QSO	z_{abs}	log N (S II)	log N (C II*)	n_e (cm^{-3})[a]	n_H (cm^{-3})
Q 0013 − 004	1.966 79$^+$	14.27 ± 0.05	....	2.7×10^{-2}	....
	1.968 22$^+$	14.16 ± 0.02	....	4.9×10^{-2}	....
	1.972 80$^+$	14.15 ± 0.06	....	3.8×10^{-2}	....
	1.972 96$^+$	14.75 ± 0.03	....	2.3×10^{-2}	....
	1.973 16$^+$	13.91 ± 0.05	....	2.4×10^{-2}	....
	1.973 65$^+$	13.86 ± 0.08	....	1.5×10^{-2}	....
	1.973 82$^+$	14.12 ± 0.05	....	8.0×10^{-3}	....
	1.973 99$^+$	13.55 ± 0.16	....	6.9×10^{-3}	....
	1.967 37	14.24 ± 0.05	....	2.4×10^{-2}	....
	1.967 63	14.12 ± 0.07	....	2.7×10^{-2}	....
	1.971 09	14.77 ± 0.01	....	1.0×10^{-3}	....
	1.971 44	14.08 ± 0.03	....	4.3×10^{-2}	....
Q 0347 − 383	3.024 63	14.50 ± 0.03	<13.00	$<5.0 \times 10^{-4}$	<6.3
	3.024 85$^+$	14.36 ± 0.04	13.55 ± 0.23	2.3×10^{-3}	4.4 − 41.9
	3.025 01	13.51 ± 0.12	<12.72	$<4.9 \times 10^{-3}$	<32
Q 0405 − 443	2.594 40	13.91 ± 0.04	<12.41	$<3.7 \times 10^{-3}$	<6.3
	2.594 64	14.72 ± 0.02	13.09 ± 0.10	$<5.7 \times 10^{-4}$	3.0 − 7.5
	2.594 74$^+$	14.07 ± 0.09	13.20 ± 0.20	$<2.5 \times 10^{-3}$	7.7 − 57.3
	2.594 85$^+$	14.73 ± 0.02	13.25 ± 0.08	$<5.6 \times 10^{-4}$	4.5 − 10.3
Q 0551 − 366	1.961 52	14.60 ± 0.10	<12.00	3.7×10^{-3}	<0.5
	1.961 68$^+$	14.01 ± 0.27	13.93 ± 0.09	3.2×10^{-2}	123.0 − 331.8
	1.961 80	14.23 ± 0.19	<12.00	4.6×10^{-3}	<1.2
	1.962 14$^+$	*Blended*	12.58 ± 0.09	....	....
	1.962 21$^+$	*Blended*	13.36 ± 0.07	....	....
	1.962 68	14.63 ± 0.11	12.98 ± 0.08	3.0×10^{-3}	2.4 − 9.6
Q 1037 − 270	2.139 00	14.68 ± 0.02	<13.50	2.0×10^{-3}	<13.2
	2.139 40	14.23 ± 0.11	13.31 ± 0.01	5.3×10^{-3}	<14.2
Q 1232 + 082	2.337 71$^+$	15.24 ± 0.11[b]	<14.00	$<7.0 \times 10^{-2}$	<48
Q 1444 + 014	2.086 79$^+$	14.32 ± 0.05	13.12 ± 0.08	1.1×10^{-2}	0.9 − 9.9
	2.086 92$^+$	14.17 ± 0.06	12.78 ± 0.20	1.9×10^{-2}	<13.0

Note. A label '+' indicates a component in which H_2 is detected. [a]Derived from the carbon ionization equilibrium. [b]Column density of Si II is given.

Péquignot, Petitjean & Boisson (1991), we can write

$$\frac{n_e}{\Gamma} = 4.35 \times 10^{11} \frac{N(\mathrm{C\,I})}{N(\mathrm{C\,II})} \left(\frac{T}{10^4}\right)^{0.64}. \quad (5)$$

Here, Γ is the photoionization rate for C I. In the local ISM, $\Gamma_{gal} \simeq (2\text{–}3.3) \times 10^{-10}\,s^{-1}$ (Péquignot & Aldrovandi 1986). Here, we neglect the ion–molecular interaction and charge exchange reactions that may produce C I. Thus, n_e/Γ can be constrained once the temperature of the gas is known. Application of equation (5) to the cold Galactic ISM (with $T = 100$ K) has resulted in $n_e \simeq 0.14 \pm 0.07\,cm^{-3}$ (Welty, Hobbs & Morton 2002, and references therein). In the stable CNM considered by Wolfire et al. (1995), the electron density is expected to be in the range $0.01 \leqslant n_e\,(cm^{-3}) \leqslant 0.02$ for $Z = 0.1\,Z_\odot$ and dust abundance one-tenth of the Galactic ISM.

5.1 Systems with C I detections

First, we concentrate on the systems with C I detections. We estimate the electron density assuming a UV field similar to the Galactic mean field (i.e. $\Gamma_{gal} = 2.5 \times 10^{-10}\,s^{-1}$), $T = T_{01}$ for the H_2 components and $T = 100$ K otherwise. Individual values of n_e derived for these systems are given in Table 4. The electron density is in the range $0.7 \times 10^{-2} \leqslant n_e\,(cm^{-3}) \leqslant 4.9 \times 10^{-2}$. Together with n_H given in Table 3, this suggests that $n_e/n_H \leqslant 10^{-3}$ for most of the systems. Therefore, the ionization state of the gas with H_2 and C I is similar to that in the CNM in a moderate radiation field.

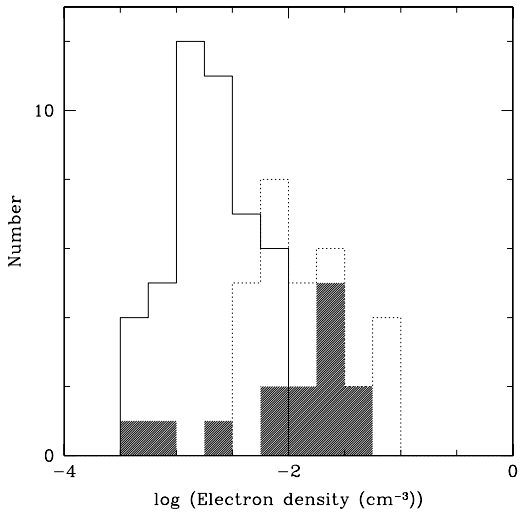

Figure 13. Histogram of the electron density derived using equation (5) for $T = 100$ K. The shaded histogram is based on systems that show detectable C I absorption lines. The histograms with continuous and dotted lines are upper limits on the electron density for systems with log N(C II) greater and less than 15, respectively. We use the C I photoionization rate given for the Galactic UV field by Péquignot & Aldrovandi (1986).

5.2 Systems without H_2 and C I

In the case of systems in which neither H_2 nor C I is detected, we assume $T = 100$ K and $\Gamma_{gal} = 2.5 \times 10^{-10}\,s^{-1}$ and obtain upper

limits on the electron density. The results are plotted in Fig. 13. We note that the inferred electron densities are much smaller than in systems in which C I (and H_2) are detected. The difference is even larger if we use only the systems with $\log N(\mathrm{C\,II}) \leqslant 15$. For this gas, the inferred electron densities are less than 10^{-2} cm^{-3} (with a median of 10^{-3} cm^{-3}). This may indicate that the absorption originates from WNM (say $T = 8000$ K). If the average radiation field in DLAs is similar to that in the Galactic ISM then the absence of C I in most of the DLAs could just be a consequence of lower densities (and/or higher T) in these systems. One can derive an independent estimate of the particle density using the excitation of C II fine structure levels. This is what we do in the following section.

6 EXCITED FINE-STRUCTURE LINE OF C II

6.1 Method to derive physical parameters

Under LTE, the column density ratio, $N(\mathrm{C\,II^*})/N(\mathrm{C\,II})$, can be written as

$$\frac{N(\mathrm{C\,II^*})}{N(\mathrm{C\,II})} = \frac{Q_{12}(\mathrm{e})n_\mathrm{e} + Q_{12}(\mathrm{H})n_\mathrm{H} + \Gamma_{12}(\mathrm{CMB}R)}{A_{21}}, \quad (6)$$

where, Q_{12} (e) $= 7.8 \times 10^{-6}$ exp$[-91.27/T]\,T^{-0.5}$ cm^{-3} s^{-1} and $Q_{12}(\mathrm{H}) = 1.3 \times 10^{-9}$ exp$[-91.27/T]$ cm^{-3} s^{-1} are the collisional excitation rates per unit volume for electrons and hydrogen atoms (Bahcall & Wolf 1968) with T being the kinetic temperature of the gas. The Einstein's coefficient is $A_{21} = 2.291 \times 10^{-6}$ s^{-1}. The CMB pumping rate, Γ_{12}(CMB), equals 6.6×10^{-11} and 1.1×10^{-9} s^{-1} for redshifts two and three, respectively (Silva & Viegas 2002). For a given temperature, the collisional excitation rate for electrons is of the order of magnitude larger than that for hydrogen atoms. For example, when $T = 1000$ K, whenever $n_\mathrm{e}/n_\mathrm{H}$ is larger than 5×10^{-3}, collisions with electrons are the dominant process. UV pumping is an additional possible excitation mechanism. For the mean radiation field in our Galaxy, the UV pumping rate is 9.3×10^{-11} s^{-1} (Silva & Viegas 2002). This is similar to or slightly lower than the CMB pumping rate for the range of redshift we consider in this study.

We compute the expected value of $\log N(\mathrm{C\,II^*})/N(\mathrm{C\,II})$ ratio under different situations and, in particular, the WNM and CNM solutions given in table 3 of Wolfire et al. (1995). Note that if CMBR pumping alone is responsible for the excitation, the expected ratios are -4.54 and -3.31 for $z_\mathrm{abs} = 2$ and 3, respectively. For the standard ISM (with stable pressure in the range 990–3600 cm^{-3} K), we derive $-2.62 \leqslant \log N(\mathrm{C\,II^*})/N(\mathrm{C\,II}) \leqslant -2.20$ for the CNM and $-3.65 \leqslant \log N(\mathrm{C\,II^*})/N(\mathrm{C\,II}) \leqslant -3.17$ for the WNM. As the DLA gas has low metallicity and low dust content, the expected pressure should be higher in the two DLA phases (see Liszt 2002; Wolfe et al. 2003a,b). If we assume $Z = 0.1\,\mathrm{Z}_\odot$ and dust-to-gas ratio one-tenth of the ISM value (which is typical of DLAs), then we expect $-2.26 \leqslant \log N(\mathrm{C\,II^*})/N(\mathrm{C\,II}) \leqslant -2.08$ for the CNM and $-3.39 \leqslant \log N(\mathrm{C\,II^*})/N(\mathrm{C\,II}) \leqslant -2.70$ for the WNM in DLAs. Thus, if DLAs originate from H I gas in a two-phase equilibrium, we expect the CMBR pumping to be subdominant compared to collisional excitation. In fact, if the gas is completely neutral then from equations (5) and (6) we derive

$$n_\mathrm{H} = \frac{A_{21}N(\mathrm{C\,II^*})}{\sigma_\mathrm{H}N(\mathrm{C\,II})} - \frac{\sigma_\mathrm{e}n_\mathrm{e}}{\sigma_\mathrm{H}} = \frac{A_{21}N(\mathrm{C\,II^*})}{\sigma_\mathrm{H}N(\mathrm{C\,II})} - \frac{\sigma_\mathrm{e}N(\mathrm{C\,I})\Gamma}{\sigma_\mathrm{H}\alpha_\mathrm{r}N(\mathrm{C\,II})}. \quad (7)$$

This gives an independent estimate of n_H which, by comparison with the estimate derived from the C I excitation, can lead to constraints on the radiation field. However, the ionization fraction (i.e. $n_\mathrm{e}/n_\mathrm{H}$) and the temperature of the neutral absorbing gas must be accurately determined before densities can be derived using the $N(\mathrm{C\,II^*})/N(\mathrm{C\,II})$ ratio. Indeed, the fact that in DLAs the Al III absorption profile is very similar to that of neutral or singly ionized species has been used as an evidence for the presence of ionized gas being mixed with the neutral gas in DLAs (Lu et al. 1996; Howk & Sembach 1999; Prochaska & Wolfe 1999; Wolfe & Prochaska 2000; Izotov, Schaerer & Charbonnel 2001; Vladilo et al. 2001). In the ionized gas: (i) n_e as well as T will be higher than what is expected in the warm or cold neutral gas. (ii) N(Si II) will underpredict N(C II) as the ionization corrections are different for the two species (see fig. 1 of Izotov et al. 2001). Neglecting the presence of ionized gas can artificially enhance the derived n_H values.

6.2 Frequency of C II* detection

In our sample, all the systems that show H_2 also show detectable C II* absorption line. The details of the fits to the C II* absorption line for these systems are summarized in Table 5 and are shown in Fig. 14. The components towards Q 0013 − 004 and Q 0528 − 250 are badly blended, and it is therefore not possible to fit N(C II*). We detect C II* in 7 out of the 21 DLAs that do not show H_2 absorption lines. If we also include the eight DLAs that show H_2, about 50 per cent (15 out of 29) of the DLAs in our sample show detectable C II* absorption line, which is consistent with the finding by Wolfe et al. (2003).

In Fig. 15, we plot the average (over the whole profile) $N(\mathrm{C\,II^*})/N(\mathrm{C\,II})$ ratio measured in DLAs in our sample together with the measurements by Wolfe et al. (2003a,b) against the total H I column density and the silicon metallicity. Here, we use the total column density summed over all the components. N(C II) is computed from N(Si II) assuming solar abundance ratio without any ionization correction. From the upper panel in Fig. 15, it can be seen that C II* is detected in all the systems with $\log N(\mathrm{H\,I}) \geqslant 21.0$. Interestingly, no such relationship exists between C I (or H_2) and H I. Most the systems with $\log N(\mathrm{H\,I}) \geqslant 21.0$ have $N(\mathrm{C\,II^*})/N(\mathrm{C\,II})$ consistent with what is expected in CNM. On the contrary, the measured values of $N(\mathrm{C\,II^*})/N(\mathrm{C\,II})$ in systems with lower N(H I) spread over more than an order of magnitude covering the expected ranges for WNM and CNM.

From the bottom panel, it can be seen that C II* is frequently detected in gas with high metallicity as already noted by Wolfe et al. (2003a). Most of the systems that show C II* absorption line with lower N(H I) do have statistically higher metallicity. In the whole sample, the number of systems with C II* detections that are consistent with CNM and WNM are approximately equal. Most of the upper limits on the ratio, measured in the metallicity range $-2.0 \leqslant \mathrm{Z}_\odot \leqslant -1.5$, are lower than what would be expected from CNM gas and are consistent with WNM (or low density) gas. Interestingly, these upper limits are lower than that seen in high latitude Galactic sightlines that are believed to be predominantly WNM gas. This means that the electron density (and therefore, probably the total particle density) in these DLAs is probably quite small.

6.3 Systems with H_2 detection

Systems with H_2 detection (marked as filled circles in Fig. 15) have $N(\mathrm{C\,II^*})/N(\mathrm{C\,II})$ consistent with CNM. We compute the allowed range of n_H in these components using $N(\mathrm{C\,II^*})$, N(S II), n_e from the C I excitation and $T = T_{01}$, if available, or $T = 100$ K (see equation 7). The results are summarized in column 6 of Table 4. This

Table 5. Results of Voigt profile fits to DLAs that do not show detectable H_2 absorption lines.

Quasar	log$N$ (H I)	$Z/Z_\odot$	z_{abs}	log N (C I)	log N (Si II)	log N (S II)	[Fe/X]	log N (C II*)	b (km s^{-1})	X
Q 0000 − 263	21.40 (0.08)	−2.06(0.09)	3.39 013	....	15.06(0.02)	14.70(0.03)	+0.03(0.06)	....	10.0(0.3)	Zn
Q 0010 − 002	20.95 (0.10)	−1.43(0.11)	2.02 471	<12.15	14.90(0.05)	14.50(0.05)	+0.18(0.08)	<13.40	5.5(0.4)	Zn
			2.02 484	<12.15	15.09(0.03)	14.77(0.03)	+0.15(0.07)	<13.40	8.4(0.5)	Zn
Q 0058 − 292	21.10 (0.10)	−1.53(0.10)	2.67 123	<12.35	14.87(0.07)	14.61(0.03)	−0.69(0.05)	12.82(0.04)	8.7(0.7)	Zn
			2.67 142	<12.35	14.98(0.05)	14.63(0.03)	−0.13(0.04)	12.79(0.04)	8.2(0.2)	Zn
Q 0102 − 190	21.00 (0.08)	−1.90(0.09)	2.36 958	<12.30	....	13.93(0.04)	−0.16(0.06)	$<12.92^{+}$	2.0(0.2)	S
			2.36 966	<12.30	....	14.06(0.03)	−0.17(0.04)	$<13.02^{+}$	3.5(0.2)	S
Q 0112 − 306	20.50 (0.08)	−2.43(0.09)	2.41 844	<12.32	13.31(0.02)	<14.14	−0.15(0.04)	<13.20	3.5(0.2)	Si
			2.41 861	<12.32	13.33(0.02)	<14.14	−0.33(0.09)	<13.20	6.9(0.4)	Si
			2.41 869	<12.32	<12.44	<14.14	> +0.33	<13.20	5.6(1.1)	Si
	20.30 (0.10)	−0.50(0.15)	2.70 111	<12.20	<14.20	....	> −0.61	<13.20	7.2(0.8)	Si
			2.70 163	<12.20	14.75(0.05)	....	−0.48(0.06)	<13.00	27.4(2.2)	Si
			2.70 217	<12.20	14.76(0.10)	....	−0.66(0.15)	<13.00	14.9(3.1)	Si
			2.70 233	<12.20	14.29(0.18)	....	−0.21(0.22)	12.60 ± 0.08	3.6(1.2)	Si
			2.70 257	<12.20	14.58(0.05)	....	−0.47(0.06)	12.97 ± 0.06	11.0(1.2)	Si
			2.70 276	<12.20	<14.20	....	> −0.43	<12.60	3.8(0.7)	Si
			2.70 316	<12.20	13.82(0.01)	....	−0.40(0.06)	12.75±0.06	7.2(1.0)	Si
			2.70 332	<12.20	14.18(0.03)	....	−0.66(0.10)	13.20±0.04	4.6(0.5)	Si
			2.70 334	<12.20	14.21(0.01)		−1.00(0.10)	13.71±0.02	11.8(1.1)	Si
Q 0112 + 029	20.90 (0.10)	−1.32(0.15)	2.42 234	<11.78	13.92(0.13)	....	−0.18(0.13)	12.56(0.24)	4.7(0.3)	S
			2.42 248	<11.78	14.04(0.11)	....	−0.35(0.12)	12.14(0.72)	6.8(0.8)	S
			2.42 266	<11.78	14.02(0.10)	....	−0.58(0.11)	12.21(0.59)	6.1(0.9)	S
			2.42 277	<11.78	14.16(0.08)	....	−0.37(0.09)	12.70(0.17)	3.7(0.3)	S
			2.42 298	<11.78	14.77(0.04)	....	−0.40(0.05)	13.66(0.06)	10.5(0.5)	S
			2.42 323	<11.78	14.65(0.04)	....	−0.38(0.05)	13.26(0.07)	6.3(0.3)	S
			2.42 338	<11.78	14.04(0.14)	....	−0.33(0.15)	13.20(0.08)	9.5(1.3)	S
			2.42 353	<12.22	13.97(0.06)	....	−1.13(0.09)	12.61(0.20)	2.5(0.6)	S
Q 0135 − 273	21.00 (0.10)	−1.40(0.10)	2.79 948	<12.00	13.91(0.05)	....	−0.27(0.07)	12.78(0.25)	7.4(1.1)	S
			2.79 960	<12.00	14.14(0.10)	....	−0.33(0.12)	13.50(0.09)	0.1(0.1)	S
			2.79 972	<12.00	14.14(0.31)	....	−0.24(0.32)	13.39(0.12)	8.4(1.4)	S
			2.79 982	<12.00	14.08(0.30)	....	−0.24(0.32)	13.38(0.12)	5.5(1.0)	S
			2.79 998	<12.00	13.85(0.10)*	....	0.39(0.11)	13.69(0.06)	6.2(0.8)	S
			2.80 010	<12.00	14.05(0.38)*	....	0.08(0.38)	13.26(0.10)	3.9(0.4)	S
			2.80 025	<12.00	14.71(0.08)	....	−0.53(0.08)	13.85(0.07)	5.1(0.2)	S
Q 0405 − 443	21.15 (0.15)	−1.41(0.15)	2.54 967	<11.70	12.99(0.27)	....	−0.84(0.82)	11.83(0.29)	0.3(0.1)	S
			2.54 973	<11.70	13.23(0.03)	....	−0.19(0.04)	12.75(0.05)	9.8(0.9)	S
			2.54 992	<11.70	14.56(0.02)	....	−0.23(0.02)	13.12(0.03)	5.3(0.2)	S
			2.55 011	<11.70	14.41(0.05)	....	−0.19(0.05)	13.21(0.04)	18.5(2.1)	S
			2.55 049	<11.70	13.76(0.11)	....	−0.09(0.12)	12.45(0.12)	9.4(2.2)	S
			2.55 060	<11.70	13.87(0.05)	....	−0.31(0.06)	12.38(0.07)	3.8(0.6)	S
			2.55 078	<11.70	14.10(0.05)	....	−0.48(0.06)	12.96(0.09)	7.8(1.3)	S
			2.55 087	<11.70	14.18(0.12)	....	−0.26(0.12)	13.16(0.12)	6.2(1.4)	S
			2.55 097	<11.70	14.30(0.06)	....	−0.31(0.06)	13.08(0.09)	4.5(0.4)	S
			2.55 105	<11.70	13.69(0.05)	....	−0.19(0.07)	12.75(0.03)	5.1(0.5)	S
			2.55 124	<11.70	13.86(0.03)	....	−0.29(0.04)	12.55(0.03)	5.9(0.5)	S
	20.45 (0.10)	−2.04(0.11)	2.62 101	<11.64	12.92(0.02)	<13.37	−0.23(0.04)	<11.75	7.5(0.2)	Si
			2.62 140	<11.64	13.20(0.03)	<13.37	−0.23(0.04)	<11.75	5.4(0.2)	Si
			2.62 158	<11.64	13.47(0.02)	<13.37	−0.28(0.03)	<11.75	16.0(0.6)	Si
			2.62 178	<11.64	12.92(0.02)	<13.67	−0.22(0.04)	<11.75	4.4(0.2)	Si
			2.62 219	<11.64	12.02(0.05)	<13.67	<+0.18	<11.75	5.7(1.3)	Si
			2.62 235	<11.64	11.87(0.06)	<13.67	<+0.33	<11.75	2.0(1.3)	Si
			2.62 287	<11.64	12.98(0.02)	<13.24	−0.55(0.06)	<11.75	10.9(0.5)	Si
			2.62 311	<11.64	13.03(0.08)	<13.24	−0.55(0.12)	<11.75	6.9(0.9)	Si
			2.62 320	<11.64	12.96(0.08)	<13.24	−0.55(0.13)	<11.75	3.6(0.3)	Si
Q 0841 + 129	21.05 (0.10)	−1.59(0.10)	2.37 439	<12.21	....	14.26(0.18)	−1.14(0.20)	12.91(0.14)	9.0(2.3)	S
			2.37 455	<12.21	....	14.43(0.12)	−0.60(0.23)	13.01(0.11)	7.2(1.3)	S
	20.80 (0.10)	−1.60(0.10)	2.47 604	<12.21	....	13.47(0.27)	−0.51(0.34)	<12.70	5.1(2.4)	S
			2.47 621	<12.21	....	14.42(0.05)	−0.26(0.07)	<12.70	9.1(1.1)	S
			2.47 642	<12.21	....	13.35(0.27)	−0.40(0.30)	<12.70	2.2(2.5)	S
Q 1037 − 270	19.70 (0.05)	−0.31(0.06)	2.13 910	12.51(0.02)	15.10(0.02)	14.65(0.01)	−0.20(0.03)	< 13.50	15.6(0.2)	Zn
			2.13 951	12.46(0.02)	14.70(0.02)	14.23(0.01)	−0.05(0.04)	< 13.08	8.8(0.2)	Zn
Q 1101 − 264	19.50 (0.04)	−1.07(0.06)	1.83 817	<11.68	12.29(0.09)	<13.05	−0.85(0.18)	<11.83	4.5(0.4)	Si
			1.83 831	<11.68	12.68(0.05)	<13.05	−0.75(0.09)	<11.83	10.3(0.3)	Si

Table 5 – *continued*

Quasar	log N (H I)	$Z/Z_\odot$	z_{abs}	log N (C I)	log N (Si II)	log N (S II)	[Fe/X]	log N (C II*)	b (km s^{-1})	X
			1.83 854	<11.68	13.33(0.02)	13.19(0.26)	−0.49(0.02)	<11.83	5.8(0.1)	Si
			1.83 871	<11.68	13.21(0.02)	13.12(0.36)	−0.49(0.03)	<11.83	9.4(0.2)	Si
			1.83 890	<11.68	13.61(0.02)	13.32(0.19)	−0.45(0.02)	<11.83	5.4(0.1)	Si
			1.83 915	<11.68	12.77(0.05)	<13.05	−0.23(0.05)	b	5.6(0.2)	Si
			1.83 925	<11.68	12.50(0.28)	<13.05	−0.15(0.28)	b	2.0(0.2)	Si
			1.83 933	<11.68	12.44(0.26)	<13.05	−0.42(0.26)	b	5.0(0.5)	Si
Q 1117 − 134	20.95 (0.10)	−1.42(0.14)	3.35 027	<12.76	14.78(0.03)	b	−0.27(0.06)	< 13.66	6.9(0.4)	Zn
			3.35 046	<12.45	14.68(0.05)	b	−0.21(0.06)	< 13.31	6.5(0.6)	Zn
			3.35 067	<12.45	14.26(0.05)	b	> −0.47	< 13.29	6.2(0.3)	Zn
Q 1157 + 014	21.80 (0.10)	−1.40(0.10)	1.94 311	<12.15	14.13(0.08)	....	−1.40(0.30)	12.36(0.14)	3.9(1.3)	Si
			1.94 318	<12.15	14.22(0.08)	....	−0.96(0.13)	12.21(0.23)	3.6(1.1)	Si
			1.94 354	<12.15	15.32(0.04)	....	−0.67(0.05)	13.91(0.04)	28.9(1.4)	Si
			1.94 346	<12.15	15.09(0.03)	....	−1.16(0.06)	13.74(0.04)	6.0(0.4)	Si
			1.94 361	<12.15	14.75(0.23)	....	−1.10(0.31)	13.00(1.37)	6.1(1.5)	Si
			1.94 375	<12.15	15.39(0.03)	....	−1.21(0.04)	14.08(0.18)	5.6(0.0)	Si
			1.94 403	<12.15	15.26(0.01)	....	−1.07(0.02)	13.87(0.02)	7.2(0.0)	Si
			1.94 385	<12.15	14.89(0.03)	....	−0.92(0.05)	13.96(0.03)	8.1(0.5)	Si
			1.94 426	<12.15	14.07(0.69)	....	....	13.14(0.06)	10.3(0.0)	Si
Q 1223 + 178	21.40 (0.10)	−1.63(0.11)	2.46 530	<12.30	14.90(0.02)	14.56(0.03)	−0.12(0.04)	13.63(0.02)	10.3(0.3)	Zn
			2.46 559	<12.30	14.78(0.03)	14.54(0.04)	+0.02(0.06)	< 13.42	14.0(0.8)	Zn
			2.46 607	<12.30	15.22(0.02)	14.82(0.02)	−0.05(0.03)	< 13.04	14.7(0.3)	Zn
			2.46 628	<12.30	14.13(0.09)	<13.85	....	<12.55	4.3(0.7)	Zn
Q 1337 + 113	20.12 (0.05)	−1.81(0.07)	2.50 766	<12.45	12.93(0.06)	b	−0.58(0.09)	<12.55	5.0(1.3)	Si
			2.50 792	<12.45	13.82(0.04)	b	−0.40(0.04)	<12.55	6.5(0.2)	Si
	21.00 (0.08)	−1.86(0.10)	2.79 557	<12.40	13.90(0.16)	....	−0.22(0.17)	b	12.8(1.6)	Si
			2.79 584	<12.40	14.63(0.04)	....	−0.34(0.04)	b	6.6(0.3)	Si
Q 1451 + 123	20.40 (0.10)	−2.27(0.14)	2.46 897	<12.75	13.23(0.09)	<13.55	−0.21(0.09)	b	6.7(0.8)	Si
			2.46 921	<12.75	13.50(0.11)	<13.55	−0.26(0.11)	b	5.7(0.5)	Si
	20.20 (0.20)	−2.10(0.21)	3.17 081	<12.65	13.31(0.06)	....	−0.29(0.14)	<13.00	9.9(1.8)	Si
			3.17 112	<12.65	13.31(0.07)	....	−0.27(0.13)	<13.00	7.3(1.5)	Si
			3.17 142	<12.65	12.72(0.18)	....	<+0.19	<13.00	9.6(4.9)	Si
Q 2059 − 360	20.29 (0.07)	−1.94(0.08)	2.50 734	<12.25	13.85(0.03)	13.49(0.23)	−0.36(0.04)	<12.53	4.5(0.3)	Si
			2.50 753	<12.25	12.99(0.10)	<13.40	−0.29(0.13)	<12.53	5.8(6.1)	Si
	20.98 (0.08)	−1.78(0.11)	3.08 261	<12.10	14.36(0.05)	13.97(0.05)	−0.29(0.05)	<12.59	5.7(0.3)	S
			3.08 291	<12.10	14.61(0.05)	14.16(0.05)	−0.25(0.05)	<12.59	8.7(0.6)	S
			3.08 314	<12.10	⩽14.27	<13.56	>−0.19	<12.59	7.2(0.9)	S
Q 2138 − 444	20.98 (0.05)	−1.74(0.05)	2.85 234	<12.02	14.86(0.02)	14.50(0.02)	−0.11(0.03)	<13.09	8.5(0.2)	Zn
Q 2332 − 094	20.50 (0.07)	−1.33(0.11)	3.05 632	<12.02	sat/bld	13.76(0.05)	−0.50(0.05)	<12.52	9.8(0.3)	S
			3.05 657	<12.02	sat/bld	13.49(0.07)	−0.51(0.08)	<12.52	5.1(0.5)	S
			3.05 676	<12.02	sat/bld	<13.42	>−0.44	<12.52	3.2(0.4)	S
			3.05 690	<12.02	sat/bld	13.48(0.11)	−0.09(0.11)	<12.52	12.9(0.6)	S
			3.05 722	<12.02	sat/bld	13.85(0.04)	−0.18(0.04)	<12.52	4.9(0.2)	S
			3.05 738	<12.02	sat/bld	13.50(0.09)	−0.55(0.10)	<12.52	6.6(0.7)	S

Note. The numbers in parentheses are 1σ standard deviations. Strict upper limits are 5σ detection limits;'....': no transition line from this ion has been observed; 'b': blended; 'sat/bld': most or all of the components in the observed transition lines from this ion are either saturated or blended or both.

table also gives upper limits on n_H for components without H_2 in systems that show H_2. It is to be remembered that we assume [C/S] in DLAs is $[C/S]_\odot$. Realistically, carbon can be under-abundant by up to a factor of 2. In that case, the density will be higher than what we quote in the table. From Tables 3 and 4, it is clear that for the H_2 components towards Q 0347 − 383, Q 0551 − 366 and Q 1232 + 082 the values of n_H derived from both the methods agree well. Such a comparison is not possible for the components towards Q 0013 − 004 and Q 0405 − 383 as C II* is blended in the former case and C I is not detected in the latter case. In the case of Q 1444+014, the derived hydrogen density based on C II* is lower than that derived using C I fine-structure excitation. However, in this system, Ledoux et al. (2003) have found a 5-km s^{-1} shift between the C I absorption line and that of singly ionized species. In addition to these components showing relative depletion of Si with respect to S, it is possible that we have overestimated N(C II). In summary, the n_H estimates based on the two methods are approximately consistent with one another. The excitation of the fine-structure levels of C I and C II in the components with H_2 detection is consistent with high-density and low-temperature CNM gas.

6.4 Systems without H_2 detection

In this section, we focus our attention on the seven systems in our sample that show C II* without H_2. These systems do not show detectable C I absorption lines except the high-metallicity system at $z_{abs} = 2.1391$ towards Tol 1037 − 270. Apart from the $z_{abs} = 1.943$ system towards Q 1157 + 014 that shows 21-cm absorption line (Wolfe, Briggs & Jauncey 1981), there is no independent constraint on T and n_H. The identification of C II* at $z_{abs} = 2.422$ towards Q 0112 + 029 and $z_{abs} = 2.799$ towards Q 0135 − 273 is based on C II*λ1037 absorption line. These lines are well inside the Lyman α

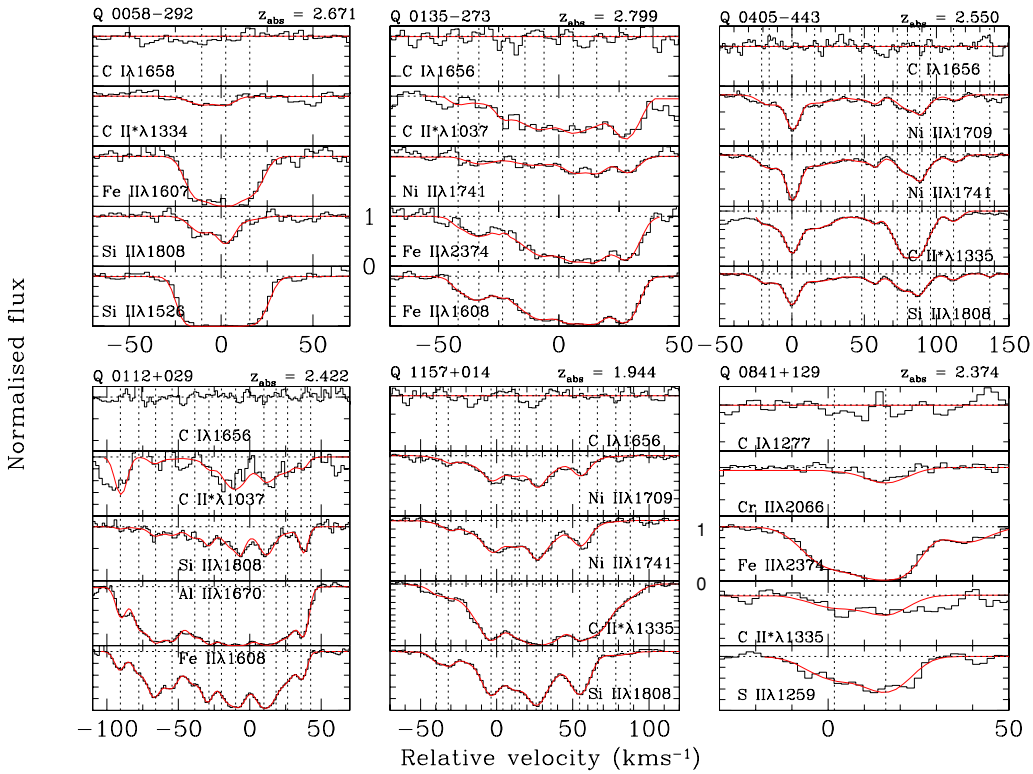

Figure 14. The Voigt profile fits to systems with C II* absorption line and without H_2 or C I absorption lines. In each panel, the histogram gives the observed spectrum, and the continuous curve is the best-fitted multicomponent Voigt profile. The vertical dotted lines mark the locations of individual components.

forest, and possible contamination by intervening H I absorption cannot be ruled out. For the rest of the systems, the identification and estimation of the C II* column density are secure.

We detect Al III absorption lines in the six (out of seven) systems for which our spectra cover the expected wavelength range of the redshifted Al III transitions. We estimate the fraction of Al in Al III using the observed metallicity and the observed N(Al III), assuming no depletion and solar relative abundances. Results are summarized in Table 6. From the table, it can be seen that 1–7 per cent of Al is ionized twice. Using photoionization models computed using the spectral synthesis code CLOUDY we derive a typical ionization parameter, $-3 \leqslant \log U \leqslant -2$, if the gas originates from a single slab irradiated by stellar spectrum with an effective blackbody temperature of 30 000–40 000 K (also see fig. 1 in Izotov et al. 2001). This implies that the average n_e/n_H ratio along the line of sight is typically in the range 0.3–0.9. Thus, there are enough electrons in the cloud so that collisions with electrons are dominant in the excitation of C II*.

The average density, n_H, is derived using equation (7) and assuming three possible combinations of T and n_e/n_H. The results are summarized in Table 6. When we use no additional constraint, the C II* observations alone are consistent with the gas having high density and low temperature (see column 4 of Table 6).

The last column in the table gives the upper limit on n_H that will keep the equilibrium abundance of H_2 below our detection limit (i.e. $N(H_2) \leqslant 10^{14}$ cm^{-2}). This value is computed using simple formation equilibrium of optically thin H_2 (Jura 1975):

$$n_H = \frac{0.11\beta(0)N(H_2)}{RN(H\,I)}, \quad (8)$$

with, R and $\beta(0)$, respectively, the formation and photodestruction rates of H_2. In the case of the ISM, $R \simeq 3 \times 10^{-17}$ s^{-1} cm^{-3} and

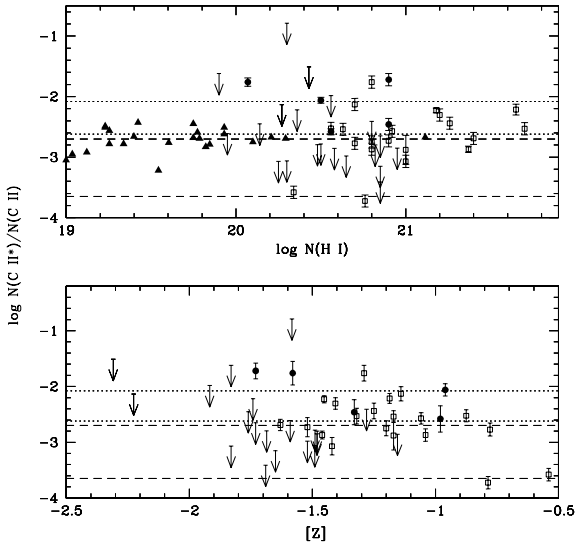

Figure 15. The average (over the whole profile) N(C II*)/N(C II) ratio in DLAs (combining our sample to measures by Wolfe et al., 2003a,b) is plotted against log$N$(H I) (upper panel) and the metallicity Z (lower panel). The dotted lines show the expected range of values observed in the CNM gas with metallicity and dust content ranging from that observed in the Galactic ISM to that of a typical DLA. The dashed lines give the corresponding range for the WNM gas. Filled circles and open squares are, respectively, for systems with and without H_2 detections. In the top panel, the filled triangles are the observations of Lehner, Wakker & Savage (2004) along high latitude Galactic sightlines with low H_2 content. Most of the points with log$N$(H I) $\leqslant$ 20.0 are from intermediate- or high-velocity clouds in the Galactic halo.

Table 6. Systems without H_2 detection.

QSO	z_{abs}	log N (Al III)	n_H (cm^{-3})			
			CNM[a]	WMN[b]	Ionized[c]	Max[d]
Q 0058 − 292	2.671	....	3.1	1.2	0.3	<3
Q 0112 − 306	2.422	−1.46	24.4	9.6	2.3	<15
Q 0135 − 273	2.799	−1.86	60.0	23.4	5.6	<5
Q 0405 − 443	2.550	−1.58	7.3	1.8	0.4	<4
Q 0841 + 129	2.374	−1.16	11.3	2.8	0.7	<22
Q 1157 + 014	1.944	−1.68	16.3	4.0	1.0	<3
Q 1223 + 178	2.465	−1.35	9.4	2.3	0.6	<2

Notes. [a] $T = 100$ K and $n_e/n_H = 0.001$. [b] $T = 8000$ K and $n_e/n_H = 0.01$. [c] $T = 10^4$ K and $n_e/n_H = 0.1$. [d] From H_2 equilibrium formation.

$\beta(0) \sim 5 \times 10^{-10}$ s^{-1}. We use the ISM value of R scaled by the dust content measured in the systems. It can be seen from Table 6 that for a moderate radiation field (like the ISM mean field), n_H, derived using C II* for the CNM-like parameters is usually higher than the upper limit obtained, based on the H_2 equilibrium formation. In addition, the expected electron density for the $T = 100$ K gas (assuming a n_e/n_H ratio as seen in CNM) is higher than 10^{-2} cm^{-3}. At such electron densities, C I should be detectable. This is inconsistent with the non-detection of C I in these systems. This problem of CNM gas producing very small amount of C I is already recognized in the literature (Liszt 2002; Wolfe et al. 2003).

We note that the absence of C I and H_2 in these systems is consistent with the gas originating either from the WNM gas or from the ionized gas. As pointed out above, the strength of the Al III absorption lines seen in these systems is consistent with the gas density being less than the one expected for the CNM.

Thus, if one uses only C II* absorption line then the results are consistent with these systems originating from CNM gas. However, the absence of H_2 and C I absorption lines together with the presence of Al III following the profiles of singly ionized gas is inconsistent with standard CNM solutions. Thus, most of the DLAs without H_2 are consistent with them originating from low-density, high-temperature and partially ionized gas.

6.5 $z_{abs} = 1.944$ towards Q 1157 + 014

Some of our conclusions of the previous section can be ascertained in the case of the $z_{abs} = 1.944$ system towards Q 1157 + 014, as we have additional information on the kinetic temperature based on 21-cm absorption (Wolfe et al. 1981). The estimated spin temperature based on the recent measurement of N(H I) is $T = 865 \pm 190$ K (Kanekar & Chengalur 2003). Fig. 16 shows the velocity plot of selected absorption lines in this system. The distribution of neutral, singly and doubly ionized species in velocity space can be visualized easily. Using a Gaussian profile, we also show, in the bottom panel, the velocity range over which 21-cm absorption is seen. Whereas, the UV absorption lines spread over more than 100 km s^{-1}, the 21-cm absorption originates from only a few of the components. There are components that do not possess 21-cm absorption but show absorption due to UV transitions including that of C II*. As expected, C II* traces a wide range of physical conditions. Assuming the temperature of the gas that is producing the 21-cm absorption feature to be 100 K (or 200 K), we can derive from the 21-cm observation the H I column density in the component lying along the line of sight: $\sim 7 \times 10^{20}$ cm^{-2} (or 1.4×10^{21} cm^{-2}). This is approximately 15 per cent (30 per cent) of the total N(H I) measured from the damped Lyman α line. This means that 85 per cent

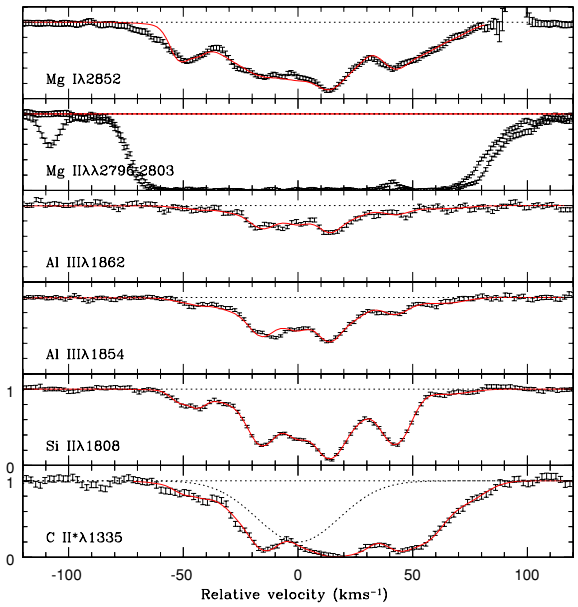

Figure 16. Velocity plot for the $z_{abs} = 1.944$ system towards Q 1157 + 014. The dotted Gaussian profile in the bottom panel is the reconstruction of the best-fitting Gaussian to the 21-cm observations of Wolfe et al. (1981). This is just to illustrate the velocity range over which cold hydrogen gas is detected.

(70 per cent) of N(H I) along the line of sight is either warm or hot. From the Si IIλ1808 profile, we note that ∼60 per cent of N(Si II) originates in the velocity space covered by the 21-cm profile. We also note that considerable fraction of Al III absorption originates from the velocity range covered by 21-cm absorption. Thus, warm and ionized components seem to be cospacial with the cold gas responsible for the 21-cm absorption. In addition, we also note that Al III components with Si II and C II* absorption are well separated from the 21-cm component. Thus, part of the C II* absorption seen here originates from the WNM or WIM. Therefore, the non-detection of H_2 in this system can be easily explained as a consequence of most of the gas being at high temperature (and hence low density). The absence of H_2 from the cold 21-cm absorbing component could just be due to the low N(H I) associated with this component and the relatively low dust depletion.

7 DISCUSSION AND CONCLUSIONS

We have studied the physical conditions in DLAs using a sample of 33 systems towards 26 QSOs acquired for a recently completed survey of H_2 in DLAs by Ledoux et al. (2003). We use standard techniques to estimate the physical conditions prevailing in the gas. In this section, we discuss some of the results and related issues.

7.1 High pressure of the H_2 gas

Our study shows that the H_2 components in DLAs trace cold gas (153 ± 78 K) with relatively high pressure. The pressure in individual components (measured assuming a radiation field similar to our Galaxy) is in the range 824–30 000 cm^{-3} K, a large fraction of the components being at high pressure. 42, 20 and 8 per cent of the components have pressure in excess of 3000 cm^{-3} K, 5000 cm^{-3} K and 10^4 cm^{-3} K, respectively. Based on the profiles of singly ionized species, we note the H_2 components arise in gas with a wide range

of molecular content and ionization state much like what we see in the Galactic ISM.

This is not unexpected. Indeed, in the framework of a Galactic two-phase medium, the stable pressure range for the gas is $460 \leqslant p/K(\mathrm{cm^{-3}\,K}) \leqslant 1750$ (Wolfe et al. 2003). Clearly, the pressure we derive in the H_2 components are much higher than this. From table 3 of Wolfire et al. (1995) it can be seen that for a given metallicity, an increase in the dust-to-gas ratio can lead to an increase in the allowed range of pressure, whereas an increase in the metallicity reduces the allowed range of pressure due to enhanced cooling. For conditions typical of DLAs, that is for metallicities of $Z = -1.0$ and a dust-to-gas ratio 10 times smaller than in the Galaxy, the stable pressure range is 1800–13 000 $\mathrm{cm^{-3}\,K}$ (Wolfire et al. 1995). Note that in the absence of any confining medium (or pressure equilibrium between different components), we expect such a high-pressure gas to survive only for a short period of time (with a typical hydrodynamical timescale of 10^6 yr).

The pressure we infer depends very much on the intensity of the radiation field. A larger intensity implies an excess of UV pumping (on top of what we assume in our analysis) which, if taken into account, should reduce the hydrogen density derived using the C I fine-structure lines. At the same time, the temperature of the gas will increase due to photoheating.

7.2 H_2 content

Ledoux et al. (2003) found that approximately 13–20 per cent of DLAs show H_2 absorption lines with most of the H_2 components having column densities in the range $16.0 \leqslant \log N(H_2)\ (\mathrm{cm^{-2}}) \leqslant 19.0$. In the case of the Galactic ISM, only a minor fraction of the clouds fall in this range. This is expected because, above $\log N(H_2) \simeq 16.0$, self-shielding drastically decreases the photodissociation rate. On the contrary, in the LMC and SMC, a large fraction of lines of sight have $16.0 \leqslant \log N(H_2) \leqslant 19.0$ (see Tumlinson et al. 2002). Thus, the trend noted in DLAs could just be a generic feature of gas with low dust content and metallicity. It is however important to remember that the molecular fraction given in Ledoux et al. (2003) is an average over the whole line of sight. The actual molecular fraction in individual components may be much larger. Thus, the low values of $N(H_2)$ that are observed could just be a consequence of low $N(\mathrm{H\,I})$ in the corresponding individual components. Indeed, consistent models of DLAs (Srianand et al. 2005) require H I column densities much less than the total $N(\mathrm{H\,I})$ measured in DLAs with H_2. In addition, the absence of 21-cm absorption can be reconciled if the H_2 components have only part of the total H I (see below).

7.3 21-cm absorption

We have shown that detecting H_2 and C I absorption lines is an efficient way to trace the cold neutral gas in DLAs. H I 21-cm absorption line provides an independent way of detecting the CNM gas in DLAs. The detectability of 21-cm absorption line depends only on the amount of cold gas along the line of sight and the covering factor of the radio source. Thus, for a compact background source, one can detect CNM gas with 21 cm without any bias from dust content or metallicity. At $z_{\rm abs} \geqslant 2$, seven systems have been searched for 21-cm absorption and none has been detected (Kanekar & Chengalur 2003). Assuming $T = 200$ K for the CNM gas, these authors estimated the filling factor of the CNM gas to be $\leqslant 0.3$. This is consistent with what we derive from our H_2 survey. Over the redshift range covered by our survey, there are three cases for which information on 21-cm absorption and H_2 content are available. To our surprise there seems to be no correlation between 21-cm absorption and H_2 absorption.

The $z_{\rm abs} = 2.811$ system towards PKS 0528 − 255 shows H_2 absorption in two distinct components without any corresponding 21-cm absorption (Carilli et al. 1996). The upper limit on τ (21 cm) gives $N(\mathrm{H\,I}) \leqslant 5 \times 10^{20}\ \mathrm{cm^{-2}}$, if the kinetic temperature is similar to T(OPR) we measure. Thus, H_2 and 21-cm observations can be consistent with one another if no more than 20 per cent of the total H I column density is associated with the H_2 component. The $z_{\rm abs} = 1.944$ system towards Q 1157 + 014 (Wolfe et al. 1981; and discussion above) and $z_{\rm abs} = 2.04$ towards PKS 0458 − 020 (Briggs et al. 1989; Ge & Bechtold 1999) show strong 21-cm absorption but no C I or H_2 absorption. In these systems, the absence of H_2 and C I absorption could be either due to low density in the cold H I component or due to the presence of higher ambient radiation field.

7.4 C II* absorption

As pointed out before, C II* is detected in all the systems in which H_2 is seen. In fact, C II* is also detected in the three systems that show 21-cm absorption discussed in the previous section. C II being the dominant ion of carbon in the neutral gas, it is natural to expect C II* associated with both 21-cm and H_2 absorption. However, C II* is readily detected in warm neutral gas and even in ionized gas. The interpretation of the origin of the C II* absorption is not as straightforward as in the case of H_2 and C I. Thus, the nature of systems that do not show 21-cm absorption and/or H_2 absorption is a matter of debate. The systems that show C II* in our sample are consistent with them originating from the CNM gas. However, the absence of C I and H_2 (if we take the depletion as an indicator of the presence of dust) and the presence of Al III are also consistent with C II* absorption originating from the warm/partially ionized gas. Thus, the frequency of occurrence of C II* provides a liberal upper limit on the CNM covering factor. A detailed investigation taking into account the constraints on the ionization state of the gas based on N II, Fe III or Al III will be important to derive the exact covering factor of CNM gas.

7.5 Star formation rate

One of the main drivers for the study of DLAs is to find out a way to recover the global star formation history in a typical, moderately star-forming environment. The importance of DLAs in the paradigm of hierarchical structure formation can be appreciated from the fact that the mass density of baryonic matter in DLAs at $z_{\rm abs} \sim 3$ is similar to that of stars at present epochs (Wolfe 1995). Studies of Lyman α and UV continuum emission from galaxies associated with DLAs usually result in SFRs (or upper limits) of a few $\mathrm{M_\odot\ yr^{-1}}$ (Bunker et al. 1999; Fynbo, Moller & Warren 1999; Kulkarni et al. 2001).

Wolfe et al. (2003a,b) have proposed a novel idea of using the C II* cooling rate to infer the SFR in DLA galaxies. The idea is that if one assumes thermal equilibrium then the cooling rate inferred from C II* should be equal to the heating rate (through UV photons, cosmic rays, etc.), driven by the local star-formation activity. Their detailed study suggests the SFR density of DLAs at high z could be as high as that inferred, based on Lyman break galaxies. We confirm the presence of C II* in $\simeq$50 per cent of the DLAs in our sample. However, it is clear from the above discussion that one needs to unveil the nature of the partially ionized gas in order to have a handle on the heating rates.

In the local Universe, star formation is always related to molecular clouds. If DLAs are star-forming regions, then the local star

formation has to be related to the mass of the molecular gas. Our survey shows that 13–20 per cent of DLAs are associated with H_2 in absorption. We have not detected CO in any of these systems, and HD is detected in only one system (Varshalavich et al. 2001). Clearly, the dark molecular clouds where stars form in our Galaxy are not seen along QSO lines of sight. The UV radiation field inferred from the H_2 high-J excitation is similar to the Galactic mean field. Following Wolfe et al. (2003a,b), the SFR per unit comoving volume for DLAs is

$$\dot{\rho}_* = An_{\rm co}(z)\langle\dot{\xi}(z)\rangle = f_{\rm d}\langle\dot{\xi}(z)\rangle\left(\frac{A}{A_{\rm p}}\right)\frac{{\rm d}N}{{\rm d}X}, \quad (9)$$

where $\langle\dot{\xi}(z)\rangle$ is the average SFR per unit area at redshift z and A, $A_{\rm p}$ and ${\rm d}N/{\rm d}X$ are average physical cross-sectional area, average projected area and number density of absorbers per unit absorption distance interval, respectively. $f_{\rm d}$ is the fraction of DLAs in which the UV radiation field is similar to the Galactic UV background (i.e. 0.13–0.20). Here we use the fact that our H_2 sample is a randomly chosen sub-sample of the whole population of DLAs, and the presence of H_2 is independent of N(H I).

For an Einstein–de Sitter cosmology, ${\rm d}N/{\rm d}X = 3 \times 10^{-5}$ for the mean redshift of our sample (Storrie-Lombardi & Wolfe 2000). Assuming $H_0 = 75$ km s^{-1} Mpc^{-1}, $A/A_{\rm p} = 2$ and $\langle\dot{\xi}(z)\rangle = 4 \times 10^{-3}\,{\rm M}_\odot\,{\rm yr}^{-1}\,{\rm kpc}^{-2}$ (typical for our Galaxy, see Kennicutt 1998) we derive $\dot{\rho}_* \geqslant 0.03$ at $z_{\rm abs} = 2.5$. This crude estimate already gives half the SFR density measured in Lyman break galaxies (Steidel et al. 1999). Recently, Hirashita & Ferrera (2005) have also arrived at similar conclusion. Thus, it is of utmost importance to understand the physics of the ISM in high-z DLAs in order to derive the cosmic star-formation budget correctly.

ACKNOWLEDGMENTS

Results presented in this work are based on observations carried out at the European Southern Observatory (ESO) under prog. ID No. 65.P-0038, 65.O-0063, 66.A-0624, 67.A-0078, 68.A-0600 68.A-0106 and 70.A-0017 with the UVES spectrograph installed on the VLT at Cerro Paranal Observatory in Chile. RS and PPJ gratefully acknowledge support from the Indo–French Centre for the Promotion of Advanced Research (Centre Franco-Indien pour la Promotion de la Recherche Avancée) under contract No. 3004-3. GJF acknowledges the support of the NSF through AST 00-71180 and NASA with grant NAG5-12020. GJF and RS acknowledge the support from the DST/INT/US(NSF-RP0-115)/2002. GS would like to thank CCS, University of Kentucky, for their 2 yr of support. The hospitality of IUCAA is gratefully acknowledged.

REFERENCES

Bahcall J. N., Joss P. C., Lynds R., 1973, ApJ, 182, 95
Bahcall J. N., Wolf R. A., 1968, ApJ, 152, 701
Bergeron J., Boissé P., 1991, A&A, 243, 344
Black J. H., van Dishoeck E. F., 1987, ApJ, 322, 412
Briggs F. H., Wolfe A. M., Liszt H. S., Davis M. M., Turner K. L., 1989, ApJ, 341, 650
Browning M. K., Tumlinson J., Shull J. M., 2003, ApJ, 582, 810
Bunker A. J., Warren S. J., Clements D. L., Williger G. M., Hewet P. C., 1999, MNRAS, 309, 875
Carilli C. L., Lane W., de Bruyn A. G., Braun R., Miley G. K., 1996, AJ, 111, 1830
Cazaux S., Tielens A. G. G. M., 2002, ApJ, 575, L29
Chaffee F. H., Foltz C. B., Black J. H., 1988, ApJ, 355, 584
Chand H., Srianand R., Petitjean P., Aracil B., 2004, A&A, 417, 853
Cui J., Bechtold J., Ge J., Meyer D. M., 2004, ApJ, in press (astro-ph/0506766)
Dalgarno A., Black J. H., Weisheit J. C., 1973, Astrophys. Lett., 14, 77
Dekker H., D'Odorico S., Kaufer A., Delabre B., Kotzlowski H., 2000, in Iye M., Moorwood A. F., eds, Proc. SPIE Vol. 4008, Optical and IR Telescope Instrumentation and Detectors. SPIE, Bellingham, p. 534
Flower D. R., Watt G. D., 1984, MNRAS, 209, 25
Forrey R. C., Balakrishnan N., Dalgarno A., Lepp S., 1997, ApJ, 489, 1000
Fynbo J. U., Moller P., Warren S. J., 1999, MNRAS, 305, 849
Ge J., Bechtold J., 1999, in Carilli C. L., Radford S. J. E., Menten K. M., Langston G. I., eds, ASP Conf. Ser. Vol. 156, Highly Redshifted Radio Lines. Astron. Soc. Pac., San Francisco, p. 121
Ge J., Bechtold J., 1997, ApJ, 477, 73
Ge J., Bechtold J., Black J. H. A., 1997, ApJ, 434, 67
Ge J., Bechtold J., Kulkarni V. P., 2001, ApJ, 547, 1
Gerlich G., 1990, J. Chem. Phys., 92, 2377
Haehnelt M. G., Steinmetz M., Rauch M., 1998, ApJ, 495, 647
Heiles C., 2001, ApJ, 551, L105
Hirashita H., Ferrera A., 2005, MNRAS, 356, 1529
Howk J. C., Sembach K. R., 1999, ApJ, 523, 141
Izotov Y. I., Schaerer D., Charbonnel C., 2001, ApJ, 549, 878
Jenkins E. B., Shaya E. J., 1979, ApJ, 231, 55
Jenkins E. B., Peimbert A., 1997, ApJ, 477, 265
Jenkins E. B., Tripp T. M., 2001, ApJ, 137, 297
Jenkins E. B., Jura M., Loewenstein M., 1983, ApJ, 270, 1
Jura M., 1975, ApJ, 197, 581
Kanekar N., Chengalur J., 2003, A&A, 399, 857
Keenan F. P., Lennon D. J., Johnson C. R., Kingston A. E., 1986, MNRAS, 220, 571
Kennicutt R. C., 1998, ApJ, 498, 541
Kulkarni V. P., Hill J. M., Schneider G., Weymann R. J., Storrie-Lombardi L. J., Rieke M. J., Thompson R. I. J., Jannuzi B. T., 2001, ApJ, 551, 37
Le Bourlot J., 2000, A&A, 360, 656
Le Brun V., Bergeron J., Boisse P., Deharveng J. M., 1997, A&A, 321, 733
Launay J. M., Roueff E., 1977, A&A, 56, 289
Lehner N., Wakker B. P., Savage B. D., 2004, ApJ, 615, 767
Ledoux C., Petitjean P., Bergeron J., Wampler E., Srianand R., 1998, A&A, 337, 51
Ledoux C., Srianand R., Petitjean P., 2002, A&A, 392, 781
Ledoux C., Petitjean P., Srianand R., 2003, MNRAS, 346, 209
Levshakov S. A., Dessauges-Zavadsky M., D'Odorico S., Molaro P., 2002, ApJ, 565, 696
Liszt H., 2002, A&A, 389, 393
Lu L., Sargent W. L. W., Barlow T. A., Churchill C. W., Vogt S. S., 1996, ApJ, 107, 475
Mandy M. E., Martin P. G., 1993, ApJS, 86, 199
Meyer D. M., Black J. H., Chaffee F. H., Foltz G., York D., 1986, ApJ, 308, 37
Morton D. C., Dinerstein H. L., 1976, ApJ, 204, 1
Péquignot D., Aldrovandi S. M. V., 1986, A&A, 161, 169
Péquignot D., Petitjean P., Boisson C., 1991, A&A, 251, 680
Péroux C., Petitjean P., Aracil B., Srianand R., 2002, New Astron., 7, 577
Petitjean P. et al., 2004, C. R. Physique, 5, 411
Petitjean P., Srianand R., Ledoux C., 2000, A&A, 364, L26
Petitjean P., Srianand R., Ledoux C., 2002, MNRAS, 332, 383
Pettini M., Smith L. J., King D. L., Hunstead R. W., 1997, 486, 665
Prochaska J., Wolfe A., 1997, ApJ, 487, 73
Prochaska J., Wolfe A. M., 1999, ApJS, 121, 369
Quast R., Baade R., Reimers D., 2002, A&A, 386, 796
Reimers D., Baade R., Quast R., Levshakov S. A., 2003, A&A, 410, 785
Roth K. C., Bauer J., 1999, ApJ, 515, 57
Roy N., Chengalur J. N., Srianand R., 2005, MNRAS, submitted
Savage B. D., Sembach K. R., 1996, ARA&A, 34, 279 J. Phys. B, 24, 2487
Savage B. D., Drake J. F., Budich W., Bohlin R. C., 1977, ApJ, 216, 291
Shaw G., Ferland G., Stancil P., Srianand R., 2004, BAAS, 36, 772
Shull J. M., van Steenberg M., 1982, ApJS, 48, 95

Silva A. I., Viegas S. M., 2002, MNRAS, 329, 135
Songaila A. et al., 1994, Nat, 371, 43
Spitzer L., Jr, Cochran W. D., Hirshfeld A., 1974, ApJS, 28, 373
Srianand R., Petitjean P., 1998, A&A, 335, 33
Srianand R., Petitjean P., 2001, A&A, 373, 816
Srianand R., Petitjean P., Ledoux C., 2000, Nat, 408, 931
Srianand R., Shaw G., Ferland G., Petitjean P., Ledoux C., 2005, MNRAS, submitted
Sternberg A., Neufeld D. A., 1999, ApJ, 516, 371
Steidel C. C., Adelberger K. L., Giavalisco M., Dickinson M., Pettini M., 1999, ApJ, 519, 1
Storrie-Lombardi L. J., Wolfe A. M., 2000, ApJ, 543, 552
Takahashi J., 2001, ApJ, 561, 254
Tiné S., Lepp S., Gredel R., Dalgarno A., 1997, ApJ, 481, 282
Tumlinson J. et al., 2002, ApJ, 566, 857
Turner J., Kirby-Docken K., Dalgarno A., 1977, ApJS, 35, 281
Varshalovich D. A., Ivanchik A. V., Petitjean P., Srianand R., Ledoux C. 2001, Astron. Lett., 27, 683
Vladilo G., Centurión M., Bonifacio P., Howk J. C., 2001, ApJ, 557, 1007
Welty D. E., Hobbs L. M., Lauroesch J. T., Morton D. C., Spitzer L., York D. J., 1999, ApJS, 124, 465
Welty D. E., Hobbs L. M., Morton D. C., 2002, ApJS, 147, 61
Wolfe A. M., 1995. in Meylan G., ed., Proc. ESO Workshop, QSO Absorption Lines. Berlin, Springer, p. 13
Wolfe A. M., Prochaska J X., 2000, ApJ, 545, 603
Wolfe A. M., Briggs F. H., Jauncey D. L., 1981, ApJ, 248, 460
Wolfe A. M., Prochaska J. X., Gawiser E., 2003a, ApJ, 593, 215
Wolfe A. M., Gawiser E., Prochaska J. X., 2003b, ApJ, 593, 235
Wolfe A. M., Howk J. C., Gawiser E., Prochaska J. X., Lopez S., 2004, ApJ, 615, 525
Wolfire M. G., Hollenbach D., McKee C. F., Tielens A. G. G. M., 1995, ApJ, 443, 152
Wolfire M. G., McKee C. F., Hollenbach D., Tielens A. G. G. M., 2003, ApJ, 587, 278

This paper has been typeset from a TEX/LATEX file prepared by the author.